IEET
International Electrical Engineering Transactions

Vol. 5 No.2 (9)
July- December, 2019
ISSN 2465-4256

An online publication of the EEAAT
Electrical Engineering Academic Association (Thailand)
www.journal.eeaat.or.th

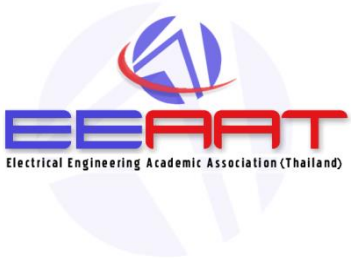

IEET – International Electrical Engineering Transactions

This journal is an online publication of the EEAAT, Electrical Engineering Academic Association (Thailand). IEET is published twice a year, ie., the first issue is for January – June and the second issue is for July – December.

EEAAT Journal Committee

IEET Editor

IEET (International Electrical Engineering Transactions) is published twice a year. Original contributions covering work in all aspects of electrical science, technology, engineering, and applications will be peer-reviewed by experts before publication. Topics of interest include the following: electrical power, electronics, telecommunication, control and system, sensor and measurement, optical technology, computer, information and communication technology (ICT), signal processing, social network tools and applications (apps), engineering education and other related fields.

For online submission of all manuscripts, correspondences, and letters, please visit
www.journal.eeaat.or.th

IEET Editorial Office

EEAAT - Electrical Engineering Academic Association (Thailand)
Room 409, F-Building,140 Cheum-Sampan Rd.
Nong Chok, Bangkok, Thailand 10530
Tel: +662-988-3655 ext 2216 Fax: +662-988-4026

IEET - International Electrical Engineering Transactions

Volume 5 (9)
Number 2
July – December 2019

PAPERS

Failure Index and Fault Determination of Power Transformer Using Fuzzy Logic and Dissolved Gas Analysis

Nitchamon Poonnoy and Cattareeya Suwanasri
Department of Electrical and Computer Engineering
Faculty of Engineering
King Mongkut's University of Technology North Bangkok
Bangkok, Thailand
nitchamonp@kmutnb.co.th and cattareeya.s@eng.kmutnb.ac.th

Thanapong Suwanasri
Electrical and Software Systems Engineering, The Sirindhorn International Thai-German Graduate School of Engineering,
King Mongkut's University of Technology North Bangkok
Bangkok, Thailand
thanapong.s.epe@tggs-bangkok.org

***Abstract*—This paper introduces fuzzy logic and dissolved gas analysis (DGA) method to fast and accurately identify the percentage failure index (%FI) and problem inside power transformer. The DGA involves Key Gas, Dörnenburg Ratio and Rogers Ratio method. Fuzzy logic with Key Gas approach is used to calculate %FI and identify problem inside power transformer while fuzzy logic with Dörnenburg Ratio and Rogers Ratio approach is used to confirm the problem. Then, the accuracy of the obtained results were verified by comparing them with the results from Duval triangle technique. Next the failure index was calculated to classify the proper maintenance actions and to effectively prioritize power transformers maintenance tasks. The maintenance task and usage strategies are also suggested in this paper. Ten power transformers were investigated. The results show that TR3 encounters the highest %FI that requires urgent investigation and corrective maintenance should be subsequently performed.**

Keywords—dissolved gas analysis, Dörnenburg Ratio, fuzzy logic, Key Gas method, failure index, Rogers Ratio.

I. INTRODUCTION

Power transformers are a key component for power transmission and distribution system. During operation it will deteriorate from either normal or abnormal condition such as heavy loaded, aging and degradation of paper-oil insulation, internal acing and partial discharge (PD), short circuit, etc. These problems directly affect to insulating oil contained inside transformer tank that acts as insulation and cooling media. The abnormal conditions cause the breakdown of hydrocarbon compound in paper-oil insulation into various gases such as methane (CH_4), ethane (C_2H_6), acetylene (C_2H_2), ethylene (C_2H_4) as well as other gases as carbon monoxide (CO), carbon dioxide (CO_2) and hydrogen (H_2). Therefore, the analysis of dissolved gases in the transformer's insulating oil can represent the health of the transformer as well as some abnormal conditions inside the transformer. This paper focuses on abnormal condition and failure identification of power transformer occurred during operation by applying dissolved gas analysis (DGA) and fuzzy logic method. The DGA including Key Gas method, Dörnenburg Ratio method and Rogers Ratio method are considered. Fuzzy logic is used as an intelligent tool to automatically identify fault type occurring inside power transformer. Samples of insulating oil collected from ten power transformers in service were analyzed and the problems inside transformer were interpreted.

The paper is organized as follows. Section II describes dissolved gas analysis technique for power transformer's insulating oil. In Section III, the fuzzy logic method applied for dissolved gas analysis is presented. Section IV presents results and analysis. Finally, the conclusions are summarized in Section V.

II. DISSOLVED GAS ANALYSIS

A. Key Gas Analysis

According to the IEEE C57-104 (1991) standard [1-2], the fault interpretation is based on key gases such as H_2, CH_4, C_2H_2, C_2H_4, C_2H_6, CO and CO_2, the problem that may occur with transformers can be identified. According to a recommendation, the Key Gas method should be used when transformer has not been analyzed for individual type of gas for a long time. The Key Gas method [2] is separated into four condition levels according to the amount of each individual dissolved gas in insulating oil, which are "good", "acceptable", "caution", and "poor" as given in Table I.

TABLE I. DISSOLVED GAS CONCENTRATION AND CONDITION CLASSISFICATION

Condition		Dissolved key gas concentration limits (ppm)						
		H_2	CH_4	C_2H_2	C_2H_4	C_2H_6	CO	CO_2
1	Good	100	120	1	50	65	350	2500
2	Moderate	101-700	121-400	2-9	51-100	66-100	351-570	2500-4000
3	Poor	701-1800	401-1000	10-35	101-200	101-150	571-1400	4001-10000
4	Bad	>1800	>1000	>35	>200	>150	>1400	>10000

For condition 1 as "Good"; if all of the key gases are in this range, transformer are in normal condition and can be operated satisfactorily. For condition 2 as "Moderate"; the key gases in this range are greater than normal condition but the transformer can be operated similarly to condition 1. For condition 3 as "Poor"; the key gases in this range have high level of decomposition, then urgent action is required. For condition 4 as "Bad"; the amount of key gases in this range indicate that there are excessive decomposition of gases inside the transformer. The transformer should be shut down and comprehensively investigated for any failure. However, by considering a combination of key gases, problem in transformer can be differentiated as described in Table II.

TABLE II. FAULT IDENTIFICATION USING KEY GAS METHOD

Key Gases	Display	Fault Types	Model Outputs
-		Normal	F1
C_2H_4 and C_2H_6	D1	Overheat oil	F2
CO and CO_2	D2	Overheat cellulose	F3
CH_4 and H_2	D3	Arcing in oil/ corona in oil	F4
C_2H_2 and H_2	D4	PD	F5

In Table II, the model output "F1" represents normal condition. All key gases are in normal condition. It implies that this transformer in this condition is satisfied. The model

outputs F2, F3, F4, and F5 show the results of combinations between two gases as C_2H_4 and C_2H_6, CO and CO_2, CH_4 and H_2, as well as C_2H_2 and H_2, which the transformer may encounter the problems as overheat oil, overheat cellulosic, arcing/corona in oil, and PD, respectively as summarized in Table II.

B. Fault Type Identification Using Dörnenburg Ratio Method

Dörnenburg Ratio method [3-5] proposes four gas ratios as r1, r2, r3, and r4 of CH_4/H_2, C_2H_2/C_2H_4, C_2H_2/CH_4 and C_2H_6/C_2H_2, respectively in order to identify a type of fault inside power transformer such as thermal decomposition, corona or low intensity PD, and arcing or high intensity PD as given in Table III. However, this method should be jointly considered with the Key Gas method to identify the severity of fault.

TABLE III. FAULT IDENTIFICATION USING DÖRNENBURG RATIO METHOD

Faults	r1	r2	r3	r4
	CH_4/H_2	C_2H_2/C_2H_4	C_2H_2/CH_4	C_2H_6/C_2H_2
Thermal decomposition	>0.1	<0.75	<0.3	>0.4
PD or low-intensity PD	<0.1	insignificant	<0.3	>0.4
Arcing or high-intensity PD	>0.1 to <1.1	>0.75	>0.3	<0.4

C. Fault Type Identification Using Rogers Ratio Method

Rogers Ratio method [3-5] introduces three gas ratios of R1, R2, and R3 as C_2H_2/C_2H_4, CH_4/H_2 and C_2H_4/C_2H_6 to identify five different fault types as low energy density and arcing PD, arcing high energy discharge, low temperature thermal, thermal is lower than 700℃, and thermal is greater than 700℃ as expressed in Table IV.

TABLE IV. FAULT IDENTIFICATION USING ROGERS RATIO METHOD

Case	R1	R2	R3	Possible Faults
	C_2H_2/C_2H_4	CH_4/H_2	C_2H_4/C_2H_6	
0	<0.1	>0.1 to 1.0	<1.0	Unit normal
1	<0.1	<0.1	<1.0	Low energy density arcing PD
2	0.1 to 0.3	0.1 to 1.0	>3.0	Arcing high energy discharge
3	<0.1	>0.1 to <1.0	1.0 to 3.0	Low temperature thermal
4	<0.1	>1.0	1.0 to 3.0	Thermal <700℃
5	<0.1	>1.0	>3.0	Thermal >700℃

III. CONDITION INDEX DETERMINATION USING FUZZY LOGIC AND DGA

A. Fuzzy Logic Approach [6-7]

Each fuzzy consists of five sets of normal member functions. This function is used to calculate fuzzy member values using two Gaussian member function (gauss2mf) as in Eq. (1).

$$f(\chi;\sigma,c) = e^{\frac{-(\chi-c)^2}{2\sigma^2}} \quad (1)$$

The function set developed for each input is a combination of σ and c parameters, where first function, χ=1, specified by σ_1 and c_1, is used to determine the shape of the left-most curve; the second function, χ=2, specified by σ_2 and c_2, is used to determine the shape of the right-most curve. Result of fuzzification from each input is then applied with fuzzy operator in the antecedent and related to the consequence which is the output of the function. Centre-of-gravity is widely used in fuzzy models for defuzzification method, where the desired output z_0 is calculated as given in Eq. (2) [14].

$$z_0 = \frac{\int z\mu_c(z)dz}{\int \mu_c(z)dz} \quad (2)$$

where $\mu_c(z)$ is the membership function of the output.

A set of fuzzy logic rules in the form of (if-and-then) statements relating the input variables to the output is developed based on transformer's diagnostic [8-10] and test data interpretation techniques. The overall fuzzy logic model comprises sub-models as will be elaborated below [11-12]. The first sub-model is described in details. Same procedure is used to create other models.

B. Fuzzy Logic with Key Gas Method for %FI and Fault Indentification

Different fuzzy rules based on input-output mapping are developed to check DGA test result. The fuzzy logic will perform the fuzzy rules of Key Gas method in 4 layers as shown in Fig. 1.

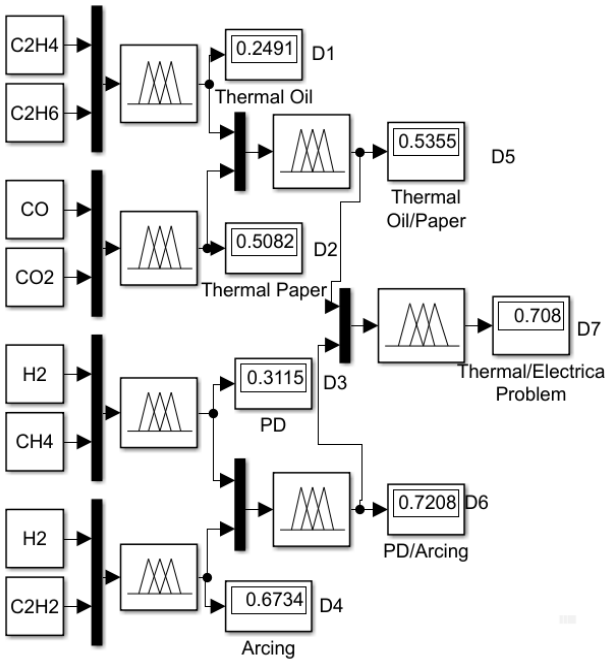

Fig. 1. Fuzzy logic flow chart using Key Gas method.

In layer 1, the key gases are matched between C_2H_4 and C_2H_6, CO and CO_2, CH_4 and H_2, and C_2H_2 and H_2, the abnormalities can be identified in terms of thermal oil, thermal cellulose or paper, PD, and arcing, which are displayed in D1, D2, D3, and D4, respectively. The problem severity can be observed by the number shown in D1 to D4 according to the range in Table V. The higher number shows higher severity of individual problem. For example, D4 presents 0.6734 that can be interpreted that this transformer encounters arcing problem inside transformer with a "caution" condition.

TABLE V. OUTPUT FUZZY RULES OF KEY GAS METHOD

Thermal Oil	Thermal paper	PD/ Corona	Arcing	Thermal oil/paper	PD/ Arcing	Condition
0-30	0-30	0-30	0-30	0-30	0-30	Good
20-55	20-55	20-55	20-55	20-55	20-55	Acceptable
45-75	45-75	45-75	45-75	45-75	45-75	Caution
75-100	75-100	75-100	75-100	75-100	75-100	Poor

TABLE VI. %FI VS CONDITION USING KEY GAS METHOD

Failure index (%FI)	Condition	Notified Color
0-25	Good	Green
26-50	Acceptable	Yellow
51-75	Caution	Orange
76-100	Poor	Red

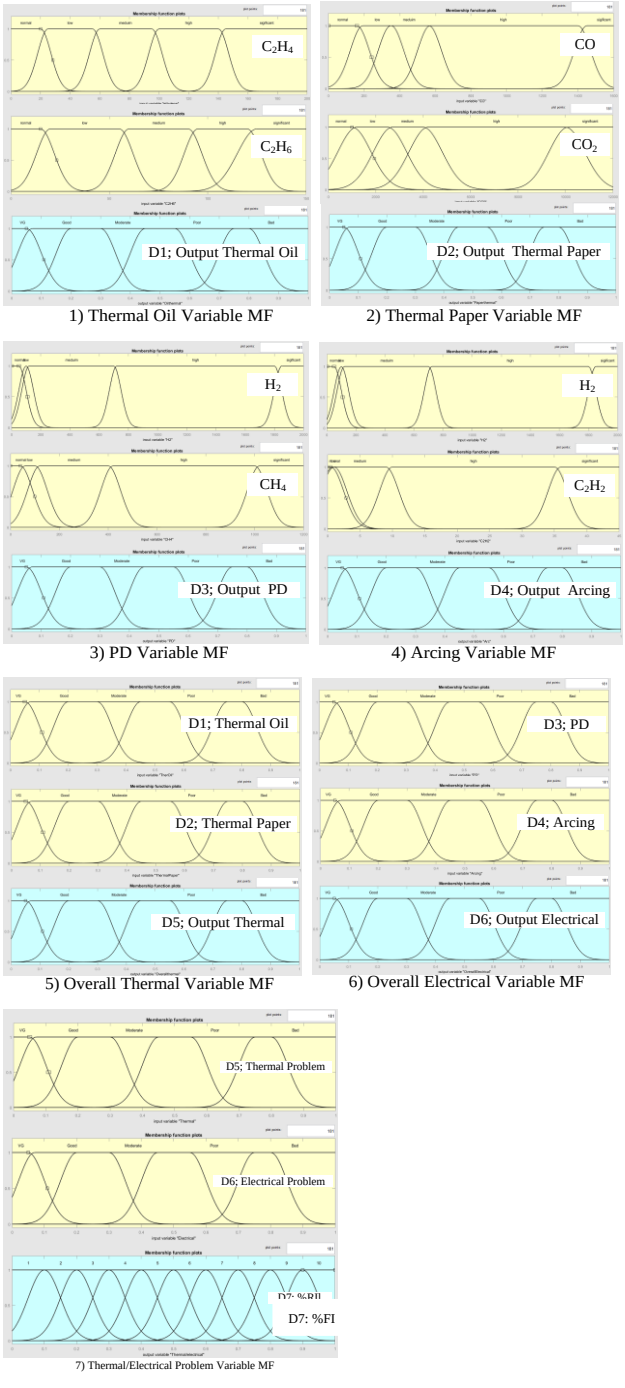

Fig. 2. Thermal/Electrical Problem Member Graph

Fig. 3 shows the member graph of each membership function according to each fuzzy rule of inputs and output (D1 to D7) by applying Key Gas method. For example, Fig. 3.1 reresents fuzzy rules of inputs and output for thermal oil problem by comparing gases C_2H_4 and C_2H_6. The result of this rule will be shown in D1.

C. Fuzzy Logic with Dörnenburg Ratio Method for Fault Identification

The set of fuzzy rules using Dörnenburg ratio method in Table III, inputs and output were developed as shown in Fig. 3 while Fig. 4 shows the member graph of each membership function according to each fuzzy rule. There is only one layer in this method, but it is a comparison of three gas ratios as r1, r2, r3, and r4 of CH_4/H_2, C_2H_2/C_2H_4, C_2H_2/CH_4 and C_2H_6/C_2H_2, respectively. According to fuzzy rules, only one output is given and then the problem such as thermal decomposition, corona or low intensity PD, and arcing or high intensity PD can be identified.

The fuzzy model is tested with input ratios r1=2, r2=0.05, r3=0.006, r4 = 1 from DGA values detected inside the transformer. Then, the fuzzy output shows "3", which is corresponding to "F2" or thermal composition according to the code interpretation in Table VII.

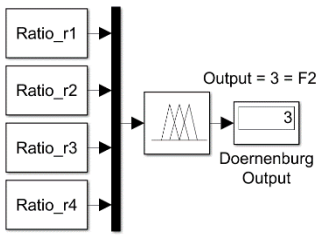

Fig. 3. Flowchart of Dörnenburg Ratio method.

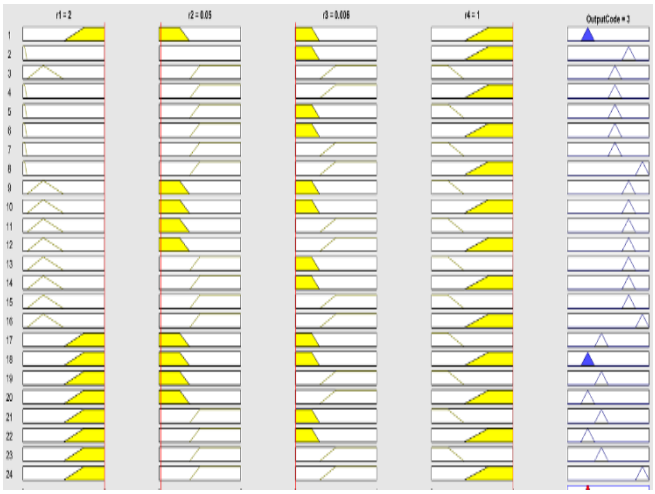

Fig. 4. Dörnenburg fuzzy rules.

TABLE VII. FUZZY CODES, OUTPUT FUNCTION AND FAULT TYPES USING DÖRNENBURG RATIO METHOD

Output Code	Output Function	Fault Types
1	F1	Normal
3	F2	Thermal composition
5	F3	Thermal composition
7	F4	Low energy electrical discharge
9	F5	High energy electrical discharge
-	F6	Out of code

D. Fuzzy Logic with Rogers Ratio Method for Fault Identification

The developed set of fuzzy rules relates the inputs to the output variable for Rogers Ratio method is shown in Fig. 6, while Fig. 7 shows the member graph of each membership function according to fuzzy rule of inputs and output. Similarly, a set of fuzzy rules using Rogers Ratio method in Table IV, inputs and output were developed as shown in Fig. 5, while Fig. 6 shows the member graph of each membership function according to each fuzzy rule. There is also one layer in this method, but it is a comparison of three ratios as R1, R2, and R3 as C_2H_2/C_2H_4, CH_4/H_2 and C_2H_4/C_2H_6 used to identify five different fault types as low energy density and arcing PD, arcing high energy discharge, low temperature thermal, thermal lower than 700℃, and thermal greater than 700℃ as mentioned in Table IV.

The fuzzy model is tested with input ratios r1=2, r2=0.05, r3=0.006, r4 = 1 from DGA values detected inside the transformer. Then, the fuzzy output shows "3", which is corresponding to "F2" or thermal fault according to the code interpretation in Table VIII.

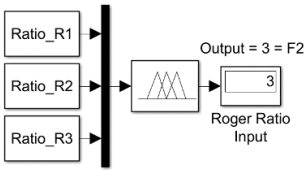

Fig. 5. Flow chart of Rogers Ratio method.

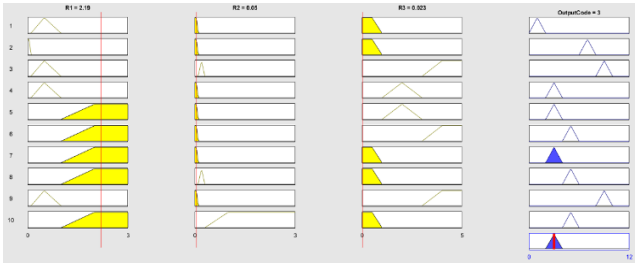

Fig. 6. Fuzzy rules Rogers Ratio method

TABLE VIII. FUZZY CODE, OUTPUT FUNCTION AND FAULT TYPE USING ROGERS RATIO METHOD

Output Code	Output Function	Fault Type
1	F1	Unit normal
3	F2	-Thermal fault <150°C -Thermal fault 150-300°C
5	F3	-Thermal fault >300°C -Thermal fault 300-700°C
7	F4	Low energy electrical discharge
9	F5	High energy electrical discharge
-	F6	Out of code

IV. RESULTS AND DISCUSSIONS

Table IX shows DGA results of ten sample transformers relating to different key gases (ppm) with their scores justified by using Key Gas method given in Table I. In Table X, after applying fuzzy logic with the Key Gas method, the results of all pairs are given from D1 to D6 while D7 shows %FI as percentage failure index of power transformer. It is found that TRs no. 2, 3, 6, 7, 9, and 10 encounter high %FI with poor condition. These results were subsequently confirmed by comparing the obtained results with the results from Duval triangle technique. The highest %FI of TR3 is equal to 87.1 % with poor condition. After back-tracking all indices of TR3 in Table X, D5=0.83 and D1=0.927 are high indices. In order to investigate problems inside power using Key Gas method, together with Dörnenburg Ratio and Rogers Ratio method, it can be concluded that TR3 encounters overheat oil with thermal fault temperature more than 300°C. The problems of other transformers are given in Table X. The fault identifications by using Key Gas, Dörnenburg Ratio, and Rogers Ratio Method of ten transformers are concluded in Table XI. In addition, the maintenance tasks and usage strategies for all transformers according to theirs condition with %FI are suggested in Table XII. For TR3, this transformer should be shut down and performed corrective maintenance.

TABLE IX. INPUT KEY GASES AND THEIR SCORES

Case Condition	Quantity of Gases (ppm)						
	H_2	CH_4	CO	CO_2	C_2H_4	C_2H_6	C_2H_2
TR1	32	36	414	4,408	16	19	2
score	1	1	2	3	1	1	2
TR2	36	79	72	1,686	10	426	0.5
score	1	1	1	1	1	4	1
TR3	35	58	91	2,362	8	204	0.5
score	1	1	1	1	1	4	1
TR4	79	40	502	3,323	33	22	11.1
score	1	1	2	2	1	1	3
TR5	11	10	232	2,608	44	19	2
score	1	1	1	2	1	1	2
TR6	31	134	151	2,532	12	502	1.5
score	1	2	1	2	1	4	2
TR7	5	85	117	2,129	30	784	0
score	1	1	1	1	1	4	1
TR8	27	0	35	170	739	209	1,224
score	1	1	1	1	4	4	4
TR9	70	21	1,094	6,558	4	16	2.5
score	1	1	3	3	4	1	2
TR10	8	169	485	9,760	174	121	0.5
score	1	2	2	3	3	3	1

TABLE X. FUZZY LOGIC RESULTS AND %FI FROM KEY GAS METHOD

Case	D1	D2	D3	D4	D5	D6	D7	%FI	Condition
TR1	0.226	0.509	0.256	0.335	0.539	0.31	0.583	58.3	Acceptable
TR2	0.927	0.268	0.313	0.318	0.773	0.291	0.869	86.9	Poor
TR3	0.927	0.325	0.283	0.318	0.83	0.324	0.871	87.1	Poor
TR4	0.249	0.508	0.311	0.673	0.535	0.72	0.708	70.8	Caution
TR5	0.264	0.341	0.224	0.335	0.316	0.31	0.362	36.2	Acceptable
TR6	0.927	0.336	0.361	0.326	0.773	0.335	0.869	86.9	Poor
TR7	0.927	0.309	0.321	0.315	0.773	0.294	0.869	86.9	Poor
TR8	0.5	0.162	0.235	0.849	0.516	0.751	0.707	70.7	Caution
TR9	0.216	0.842	0.3	0.345	0.75	0.32	0.868	86.8	Poor
TR10	0.927	0.658	0.405	0.318	0.822	0.357	0.87	87.0	Poor

TABLE XI. FAULT INDENTIFICATION BY KEY GAS, DÖRNENBURG RATIO, AND ROGERS RATIO METHOD

Case.	Key Gas	Dörnenburg Ratio	Rogers Ratio
TR1	Overheat cellulose	Thermal composition	Thermal fault <150°C
TR2	Overheat oil	Thermal composition	Thermal fault >300°C
TR3	Overheat oil	Thermal composition	Thermal fault >300°C
TR4	Overheat cellulose	Thermal composition	Thermal fault <150°C Thermal fault 300-700°C
TR5	Normal	Normal	Unit normal
TR6	Overheat oil	Thermal composition	Thermal fault >300°C
TR7	Overheat oil	Thermal composition	Thermal fault >300°C
TR8	Overheat oil + Arcing in oil	High energy electrical discharge	High energy electrical discharge
TR9	Overheat cellulose	Thermal composition	Thermal fault <150°C
TR10	Overheat oil+ Paper	Thermal composition	Thermal fault <150°C

TABLE XII. MAINTENANCE TASKS AND USAGE STRATEGIES CORRESPONDING TO THE CONDITIONS

Condition	Maintenance Task and Usage Strategies
Good	Time-based maintenance: visual inspection, dielectric breakdown voltage test, DGA, PD measurement
Acceptable	Time-based maintenance: visual inspection, dielectric breakdown voltage test, DGA, PD measurement, electrical test (turn ratio, PF, PI)
Caution	Condition-based maintenance: full electrical and insulating oil test, DGA, PD measurement, shutdown planning for repairing
Poor	Shutdown and corrective maintenance: condition monitoring, root caused analysis, maintenance setup and execution, re-condition monitoring, usage decision-making

V. CONCLUSION

The fuzzy logic approach can be used to evaluate the condition of power transformer in term of percentage of failure index and internal fault determination with the application of dissolved gas analysis technique considering Key Gas method, Dörnenburg Ratio method, and Rogers Ratio method. Fuzzy logic with Key Gas approach is used to calculate %FI and identify problem inside power transformer, while fuzzy logic with Dörnenburg Ratio and Rogers Ratio approach is used to confirm the problem. Then, the DGA test results of ten sample transformers were evaluated by using this fuzzy logic tool. Then, the accuracy of the obtained results were verified by comparing them with the results from Duval triangle technique. The result shows that the sample transformers are having an internal fault and most of fault type is thermal fault. Therefore, by using this developed fuzzy logic tool, the condition and internal problem of power transformers can be clearly identified. Then, the recommended maintenance strategy and time interval should be effectively planned to minimize the catastrophic damage, which could occur with power transformer and its network. All proposed techniques are used in practice nowadays. Furthermore, other techniques should be combined together to increase the reliability of the analysis.

REFERENCES

[1] IEEE guide for the interpretation of gases generated in oil-immersed transformers, IEEE Std. C57 104–2008 (Revision of IEEE std C57 104-1991), 2009 C1–28.

[2] R. Rogers, “IEEE and IEC codes to interpret incipient faults in transformer using gas in oil analysis,” IEEE Transactions on Dielectrics and Electrical Insulation, vol. 13, 1978, pp. 349–354.

[3] Omar M. Elmabrouk., et al. “An implementation of fuzzy logic technique for prediction of the power transformer faults,” World Academy of Science, Engineering and Technology International Journal of Mechanical and Industrial Engineering, vol.13, no.6, June 2019, pp.407-412.

[4] M. Arshad, S. M. Islam, A. Khaliq, “Fuzzy logic approach in power transformers management and decision making,” IEEE Transaction on Dielectric and Electrical Insulation, vol. 21, 2014, pp. 2343–2354.

[5] A. Siada, S. Hmood, S. Islam, “A new fuzzy logic approach for consistent interpretation of dissolved gas in oil analysis,” IEEE Transactions on Dielectrics and Electrical Insulation, vol. 20, 2013, pp. 2343-2349.

[6] Husain, Zakir, “Fuzzy logic expert system for incipient fault diagnosis of power transformers,” International Journal on Electrical Engineering and Informatics, vol. 10, no.2, 2018, pp. 300-317.

[7] N. Nedjah, L. M. Mourelle, Fuzzy systems engineering theory and practice, Springer, 2005.

[8] A. N. Jahromi, R. Piercy, S. Cress, W. Fan, “An approach to power transformer asset management using health index,” IEEE Electrical Insulation Magazine, vol. 25, 2009, pp. 20–34.

[9] Ortiz, F.; Fernandez, I., Ortiz, A.; Renedo, C.J., Delgado, F., Fernandez, C. “Health Indexes for power transformers: A case study,” IEEE Electrical Insulation Magazine. 2016, 32, 7–17.

[10] T. Suwanasri, P. Sirimongkol, C. Suwanasri and R. Phadungthin, “Software development for power transformer condition evaluation using dissolved gas analysis methods; practical experience in Thailand,” The 18th International Conference on Electrical Machines and Systems (ICEMS), Pattaya, 2015, pp. 329-333.

[11] T. Suwanasri, J. Haema, R. Phadungthin and C. Suwanasri, “Diagonostic techniques to evaluate internal condition of power transformer,” ECTI-CON, Pattaya, Thailand, May 2009.

[12] IEEE Std C57.104-1991, “IEEE Guide for the Interpretation of Gases Generated in Oil-Immersed Transformer,” 1991.

[13] Engineering Graine, L., Hossenlopp, L., et al. “Renovation /refurbishment of Substation Secondary Systems,” Cigre, Paris., 2002., pp.23-301.

[14] Amantegui, J. et al., “Utilities approach to protection and control refurbishment.” Cigre, Paris. 34-208, 2002.

Modeling and Analysis for Temporary Over Voltage of Capacitor Bank for Grid Locations connected a PV System by using PSCAD

Nattapan Thanomsat
Department Electrical Engineering, Faculty of Engineering, Burapha University
E-mail: nattapan@eng.buu.ac.th

***Abstract*— This paper introduces modeling and analysis for Temporary Over Voltage (TOV) of Capacitor Bank for grid connected a Photovoltaic (PV) system. The only way to analyze short duration phenomenon in the electric circuit is to solve the differential equations related to that system. In addition, the way PSCAD software is implemented is to solve a combination of differential equations, and, therefore, it is possible to see the effects of fast transients on the system electrical quantities. The used 22 kV distribution system model is radial network with fix load. The first simulation, PV system and Capacitor bank is connected at the low voltage side of distribution transformer. The second simulation, PV rooftop system and Capacitor bank is connected at the end of distribution line. Therefore, this analysis of system has been simulated using PSCAD/EMTDC for different phenomenon in this system.**

Keywords—Distribution network, PV Rooftop System, Temporary Overvoltage, PSCAD, CapacitorBank.

I. INTRODUCTION

The integration of photovoltaic (PV) systems into electrical power grids continues its growing pace unabated. The technological maturity nowadays accrued by solar panels is enabling PV systems to rapidly become the preferred pollutant-free energy source connected at both transmission and distribution levels [1–4]. It is estimated that, however, most grid-connected PV systems will be distributed all over the network, as opposed to having very large PV plants connected to just a few network buses; in other words, PV systems are expected to be massively integrated into existing low- and medium-voltage networks [5,6]. Admittedly, the interconnection of PV-based distributed energy resources (DER) is bringing about a wide variety of technical challenges related to the system's planning and operation, with most of them currently awaiting solution [4].

The low voltage and high current characteristics of distribution system leads to high power losses compared to that of transmission system. About 13% of total power generated is consumed as power losses at the distribution system [7]. The losses produced by reactive components of branch currents can be reduced by the installation of shunt capacitors. Capacitive compensation reduces power loss, improves voltage profile of system, increases the power factor and releases kVA capacity of distribution equipment for additional load growth [8]. M. Chakravorty, and D. Das had studied Voltage stability analysis of radial distribution networks and found that the installation of shunt capacitors reduces power loss, improves voltage profile of system, and increases the power factor on distribution system [9].

On distribution lines with industrial loads, capacitors are frequently switched by time clock in anticipation of an increase in load with the beginning of the working day. Common problems are adjustable-speed drive trips and malfunctions of other electronically controlled load equipment that occur without a noticeable blinking of the lights or impact on other, more conventional loads. That mean, capacitor switching overvoltage is that the problems appear at nearly the same time each day. D. V. Coury et al. reported Transient analysis concerning capacitor bank switching in a distribution system to discuss the impact of temporary overvoltage on distribution system [10]. M.A. Chapman et al. studied Switching and fault caused transients in electric power systems and found that the temporary overvoltage of capacitor bank switching had effected distribution system [11].

In all previous studies, possibility of the capacitor bank switching problem had been studied, also the effects of temporary overvoltage in grid connected on PV rooftop system in the case has not been investigated. In this paper, the PV rooftop system and the temporary overvoltage by capacitor bank switching on grid connected simulation are simulated and analyzed. The model system proposed in this paper is developed in simulation tool, PSCAD/EMTDC. Based on the simulation results present the voltage and the current during the transient process with and without PV rooftop system and Capacitor bank.

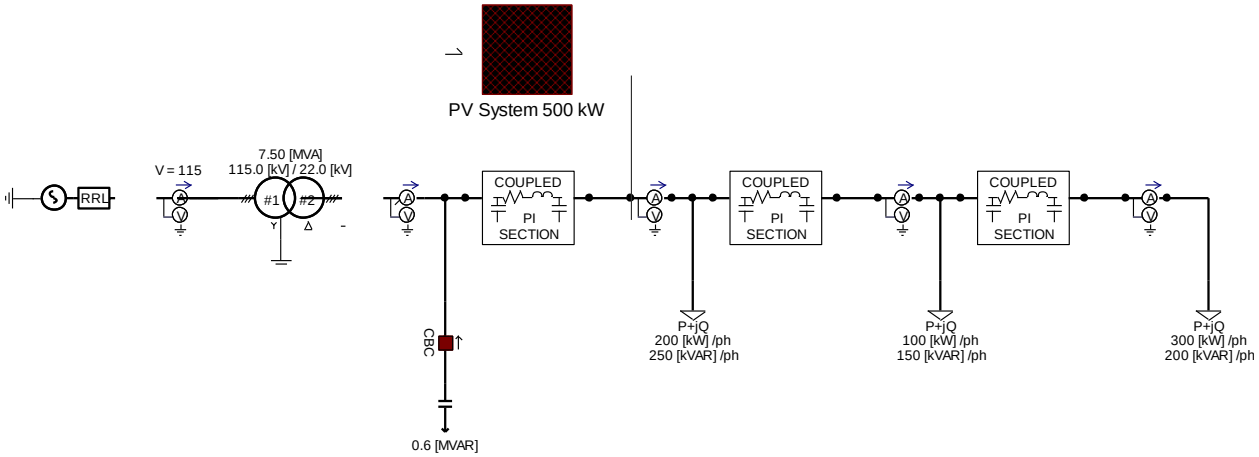

Fig. 1. Modeling distribution network with Capacitor Bank and PV system at the substation by using PSCAD/EMTDC

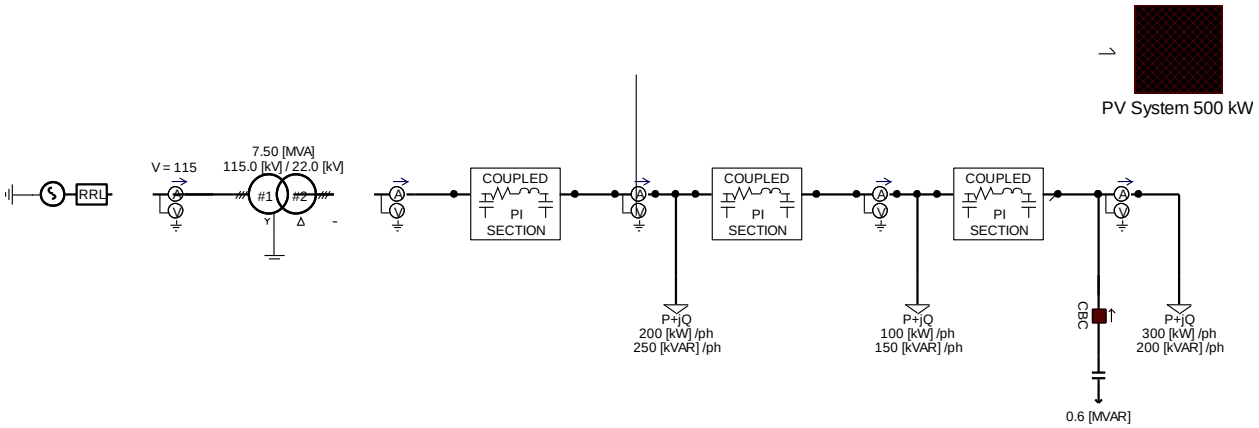

Fig. 2. Modeling distribution network with Capacitor Bank and PV system at the end of distribution line by using PSCAD/EMTDC

II. PSCAD / EMTDC MODELING

The distribution system consists of substation with transformer stepdown from 115kV to 22 kV. The distribution line contains three pieces of line with connected load, first line 3 km in length with the load of 200+250 kVA/ph, second line 3 km in length with the load of 100+150 kVA/ph, and the last 4 km in length with the load of 300+200 kVA/ph. The Capacitor bank is 0.6 MVAR and the PV system has base on 500 kW. With this data, the modeling system was operated by using PSCAD/EMTDC as shown in Fig 1 and 2. Fig. 1 shows the power flow on the system with Capacitor Bank and PV system attached to the end of substation. Fig. 2 shows the power flow on the system with Capacitor Bank and PV system attached to the end of distribution line.

III. SIMULATION AND RESULTS

. First step, the voltage profile of distribution line has been to plot without capacitor bank and PV system. The distribution line are 3 km, 3 km, and 4 km with the load each line. The voltage profile of the line will be as drawn like a blue line in Fig. 3. Second step, the PV system is operated by closed circuit, the voltage profile of the line will be as drawn like an orange line in Fig. 3. Third step, PV system is opened and the capacitor bank is closed, the voltage profile of the line will be as drawn like a gray line in Fig. 3. The last, PV system and Capacitor bank are connected at the end of substation, the voltage profile of the line will be as drawn like a yellow line in Fig. 3.

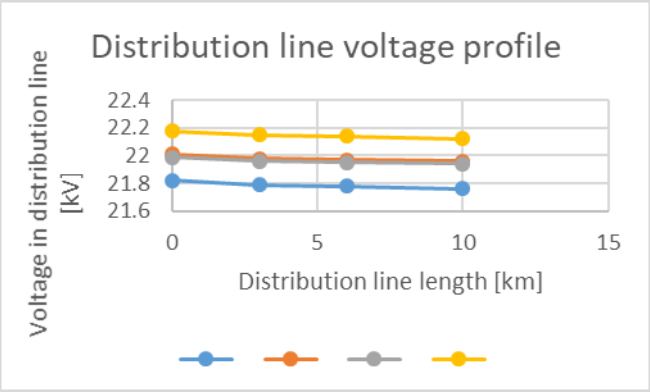

Fig. 3 Distribution line voltage profile with Capacitor Bank and PV system attached to the end of substation

The result of simulation in Fig.3 shown that the voltage decreases from the substation by increasing the length and the load. The PV system and capacitor bank are used to enhance and compensate node voltages along the distribution feeders.

Another case, the PV system and Capacitor bank are connected at the end of distribution line as one by one. The last. they are connected together. The voltage profile of the line without PV system and capacitor bank will be as drawn like a blue line in Fig. 4. The voltage profile of the line with PV system will be as drawn like an orange line in Fig. 4. The voltage profile of the line with capacitor bank will be as drawn like a gray line in Fig. 4. And the voltage profile of the line with both will be as drawn like a yellow line in Fig. 4.

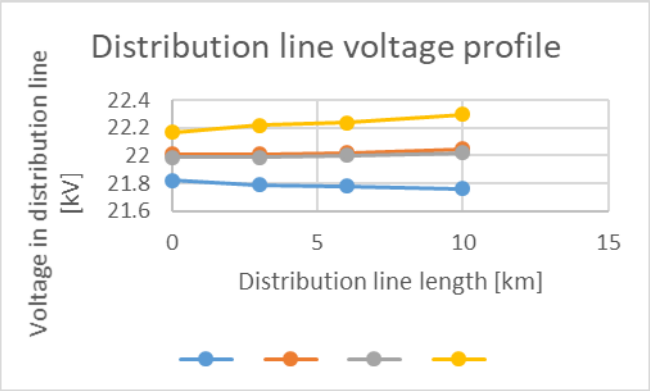

Fig. 4 Distribution line voltage profile with Capacitor Bank and PV system attached to the end of distribution line

The result of simulation in Fig.4 shown that the PV system and capacitor bank are used to enhance and compensate voltages at along the end of distribution feeders. They are useful to increased voltage in distribution and better than in Fig.3.

Occurrence of a fast transient of switching capacitor bank can induce a voltage traveling wave, with a magnitude many times higher than the system rated values. Although they may last in the order of microseconds, still the impulse voltages, better known as the temporary overvoltage (TOV), caused by the phenomenon are detrimental to personnel and equipment.

Therefore, the simulation is trying to show the effect of switching a capacitor bank in the distribution line without PV system grid connected as shown in Fig. 2. The capacitor bank of 0.6 MVAR is being switched to point at t = 2.017 sec. The maximum voltage per phase will be 17.8 kV. Fig. 5 shows the capacitor bank switching has pushed the maximum of the voltage to 22.01 kV, this means a 28.8% increase.

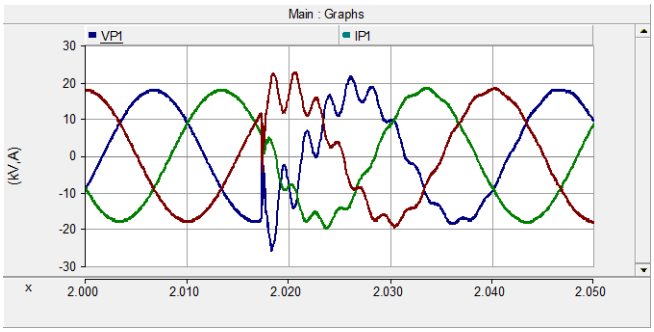

Fig.5 AC voltages measured at the end of distribution line, when capacitor switching.

Other conditions may cause temporary overvoltage. Recently with rises in PV system integrations, in case of having minimal loads and a very sunny day, the feeder prevalent of solar generation may experience dangerous voltage levels and if capacitor bank is switched, the system is caused damage. Therefore, the simulation is trying to show the effect of switching a capacitor bank in the distribution line with PV system grid connected as shown in Fig. 2. The capacitor bank of 0.6 MVAR is being switched to point at t = 2.19 sec. The maximum voltage per phase will be 18.02 kV. Figure 6 shows the capacitor bank switching has pushed the maximum of the voltage to 25.76 kV, this means a 42.95% increase.

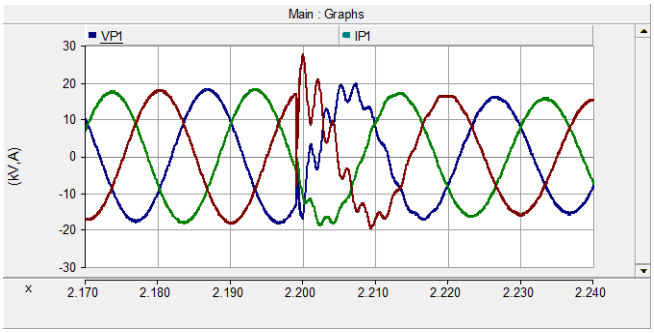

Fig.6 AC voltages measured at the end of distribution line with PV system grid connected, when capacitor switching.

IV. CONCLUSION

From simulation and analysis of Temporary Over Voltage of Capacitor Bank for Grid Locations connected a PV System by creating a model using PSCAD program, it is found that Many factors in a distribution system result in voltage levels that either too far below scheduled voltage levels. Transmitting current over long distances results in voltage drops due to losses over lines. Also in many applications in industry zone, such as inductive machines, inevitable. The voltage at the end of the feed line will be greatly reduced compared to the beginning of the line. Therefore, power users at the end of the line will encounter problems with insufficient voltage. One basic tool used for voltage level correction is capacitor banks. During normal operation, the level of the reactive power in a distribution system is the main controller of voltage level. This is because voltage levels are directly proportional to the reactive power in a grid. So, Voltage regulating capacitor banks would then be used to compensate this voltage drop. Another way, the consumers are able to produce electricity by themselves, such as PV system, and they pay back into the distribution system, the said effect will disappear and also helps to increase the voltage stability of the distribution system. However, the distribution system consists of PV system and Capacitor bank switching, they can make happening of a fast transient voltage and can induce a voltage traveling wave, with a peak voltage many times higher than the system rated values. Although they may last in the order of microseconds, still the impulse voltages, better known as the temporary overvoltages (TOVs), caused by the phenomenon are detrimental to operated personnel and equipment. Therefore, this simulation result is essential to understand the root causes of TOVs in designing a system and provide solutions to mitigate possible TOVs.

REFERENCES

[1] Wang L, Yan R, Saha TK. Voltage management for large scale PV integration into weak distribution systems. IEEE Trans Smart Grid 2018;9(5):4128–39.

[2] Aziz T, Ketjoy N. Enhancing PV penetration in LV networks using reactive power control and on load tap changer with existing transformers. IEEE Access 2017;6:2683–91.

[3] Guggilam SS, Dall'Anese E, Chen YC, Dhople SV, Giannakis GB. Scalable optimization methods for distribution networks with high PV integration. IEEE Trans Smart Grid 2016;7(4):2061–70.

[4] Cheng D, Mather BA, Seguin R, Hambrick J, Broadwater RP. Photovoltaic (PV) impact assessment for very high penetration levels. IEEE J Photovolt 2016;6(1):295–300.

[5] Nanou SI, Papathanassiou SA. Modeling of a PV system with grid code compatibility. Electr Power Syst Res 2014;116(Nov):301–3010.

[6] Haque MM, Wolfs P. A review of high PV penetrations in LV distribution networks: Present status, impacts and mitigation measures. Renew Sust Energy Rev 2016;62(May):1195–208.

[7] H.N. Ng, M.M.A. Salama, A.Y. Chikhani "Classification of capacitor allocation techniques" IEEE Trans Power Del, 15 (1) (2000), pp. 387-392.

[8] N.Gnanasekaran, S.Chandramohan P.SathishKumar, and A.Mohamed Imrand "Optimal placement of capacitors in radial distribution system using shark smell optimization algorithm" Ain Shams Engineering Journal Volume 7, Issue 2, June 2016, Pages 907-916.

[9] M. Chakravorty, D. Das "Voltage stability analysis of radial distribution networks" Electr Power Energy Syst, 23 (2001), pp. 129-135.

[10] Denis V Coury, Cláudio José dos Santos, Mário Oleskovicz, Maria Cristina Tavares, "Transient analysis concerning capacitor bank switching in a distribution system", Electric Power Systems Research, vol. 65, pp. 13, 2003.

[11] M.A. Chapman, A. Martinez, E. Sabir, K. Wang, Y. Liu, "Switching and fault caused transients in electric power systems", Power Engineering Society 1999 Winter Meeting IEEE, vol. 2, pp. 1015-1021 vol.2, 1999.

Simulation and Comparison of SPWM and SVPWM Techniques for PMSM Drives

Wisaruda Suppharangsan and Anuparp Boonsongsrikul
Department of Electrical Engineering, Faculty of Engineering, Burapha University
E-mail: wisaruda@eng.buu.ac.th

ABSTRACT — This paper presents the comparison between Sinusoidal Pulse Width Modulation (SPWM) and Space Vector Pulse Width Modulation (SVPWM) by using motor characteristics of PMSM motor. The focus is based on the same torque load and the same motor speed with these modulation approaches. The results show that THD and the peak phase voltage from both methods are similar. These are different from comparison with the same modulation index.

Keywords: *PMSM, SPWM, SVPWM, total harmonic distortion, modulation schemes.*

I. INTRODUCTION

Permanent magnet synchronous motors (PMSM) are widely used in many applications such as electric vehicles, robotics, and washing machines. They have small sizes, high torque density, low inertia and low maintenance [1]. PMSMs also have high power factor because there is no need for magnetizing current and they are high efficiency due to no rotor copper loss. For supplying the power to PMSM, three-phase voltage source inverter (VSI) is mainly used [2]. In Fig.1, the diagram of two-level VSI circuit is illustrated. VSI cooperates with the modulation methods of which construct variable voltages and variable frequency to PMSM.

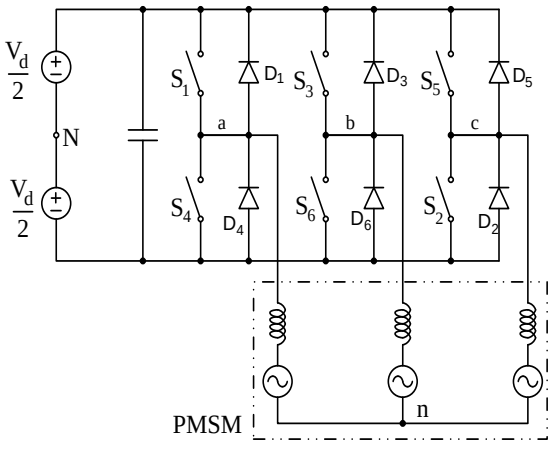

Fig. 1 Three-phase Two-Level VSI

There are 2 widely used methods with carriers. They are sinusoidal pulse width modulation (SPWM) and space vector pulse width modulation (SVPWM). SPWM is the most widely used method because it is easy to implement and it is compatible with many applications [3]. Nevertheless, SVPWM provides better features. Although SVPWM has complex computation process, there are several benefits. For examples, the maximum output voltage of SVPWM at the fundamental frequency is greater that of SPWM by 15.5% [1-7]. The switching time of SVPWM is less than that of SPWM around 30% [4].

The comparison of modulation methods are reported in several papers [1-4]. Other than the previous descriptions, SVPWM is claimed that the harmonic contents of the voltage and current output are less than those of SPWM [7-8]. These are analyzed on the base that the modulation index of SPWM and that of SVPWM are the same. However, most applications of PMSM are applied to loads. Therefore, for the reasonable comparison between SPWM and SVPWM, both methods should be compared on the basis of the same toque load and the same machine speed. In this paper, the principles of conventional SPWM and space vector PWM approaches are described. After that, the comparative analysis of the response characteristics between two methods at the same loads and the same speeds is shown.

II. SINUSOIDAL PULSE WIDTH MODULATION

SPWM is stand for "Sinusoidal Pulse Width Modulation". It functions to generate sinusoidal signals in the form of various widths of rectangular pulses. This modulation method is simple and easy to implement. The principles of the three-phase SPWM is that the three sinusoidal reference signals are compared with a triangular carrier wave. As shown in Fig.2, from phase A of the VSI, when the sinusoidal wave is greater than the triangular waveform, the upper switch of phase A (S1) is turned on and the lower switch of phase A (S4) is turned off. On the other hand, when the sinusoidal wave is smaller than the triangular waveform, the lower switch of phase A (S4) is turned on and the upper switch of phase A (S1) is turned off.

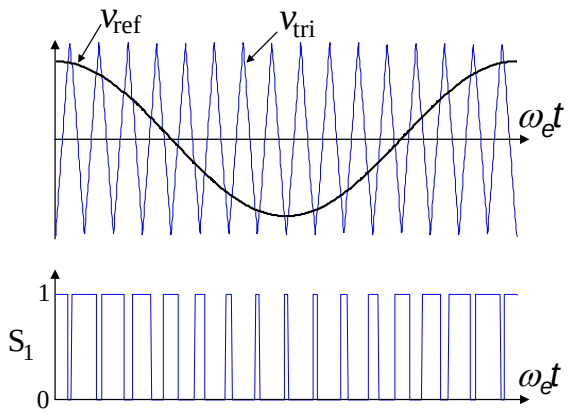

Fig. 2 Phase-a sinusoidal wave comparing with triangular wave

III. SPACE VECTOR PULSE WIDTH MODULATION

SVPWM is a switching scheme, which is produced from rotating magnetic field concept. The magnetic vectors from three-phase currents are summed as one rotating magnetic space vector. The three-phase magnetizing current are substituted by three-phase voltages, as

$$\begin{aligned} v_a &= V_m \sin \omega t \\ v_b &= V_m \sin\left(\omega t - 120^\circ\right) \\ v_c &= V_m \sin\left(\omega t + 120^\circ\right) \end{aligned} \tag{1}$$

Then, these three-phase voltage are converted to three vectors by multiplied by unit vectors.

$$\begin{aligned} \vec{V}_a &= v_a 1 \\ \vec{V}_b &= v_b \alpha \\ \vec{V}_c &= v_c \alpha^2 \end{aligned} \tag{2}$$

where α is unit vector at $\frac{2\pi}{3}$ rad, which is $e^{j\frac{2\pi}{3}}$.

While all three vectors are combined, the rotating space vector is derived as,

$$\vec{V}_{ref} = \frac{2}{3}\left(\vec{V}_a + \vec{V}_b + \vec{V}_c\right) \tag{3}$$

This space vector as reference vector (V_{ref}) rotates at the speed ω, as shown in Fig 3. The space vector (V_{ref}) can be broken into 2 vector components, V_d and V_q, which are perpendicular to each other and also rotate at speed ω, as illustrated in Fig 4.

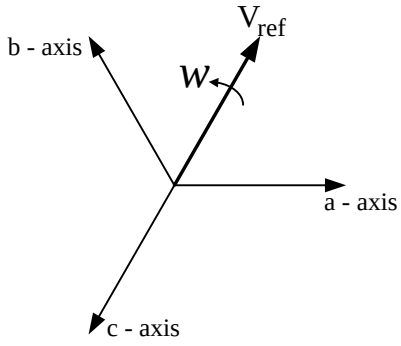

Fig. 3 Rotating voltage space vector.

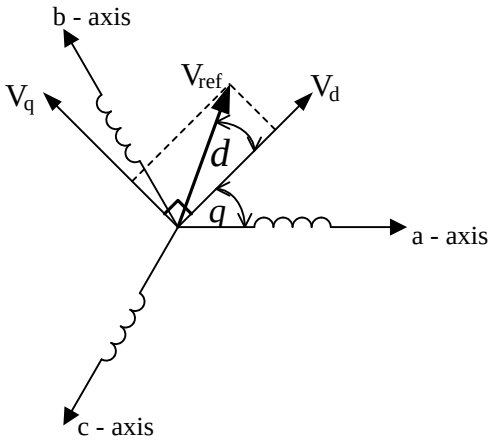

Fig. 4 Voltage space vector in dq reference frame and abc reference frame.

From Fig.4, the magnitude of V_{ref} is given by

$$\left|\vec{V}_{ref}\right| = \sqrt{\left|V_d\right|^2 + \left|V_q\right|^2} \tag{4}$$

where $\delta = \tan^{-1}\left(\frac{V_q}{V_d}\right)$ and θ is the angle of the rotor of PMSM.

From Clarke's and Park's transformation, any magnitude in abc reference frame can be converted into dq reference frame as follow,

$$\begin{bmatrix} X_d \\ X_q \end{bmatrix} = \frac{2}{3}\begin{bmatrix} \cos\theta & \cos\left(\theta - \frac{2\pi}{3}\right) & \cos\left(\theta + \frac{2\pi}{3}\right) \\ -\sin\theta & -\sin\left(\theta - \frac{2\pi}{3}\right) & -\sin\left(\theta + \frac{2\pi}{3}\right) \end{bmatrix}\begin{bmatrix} X_a \\ X_b \\ X_c \end{bmatrix} \tag{5}$$

After the magnitude and the angle of the space vector (V_{ref}) are obtained, the space vector is converted into 6-switching scheme. The space vector is placed in a voltage space vector hexagon, as shown in Fig 5.

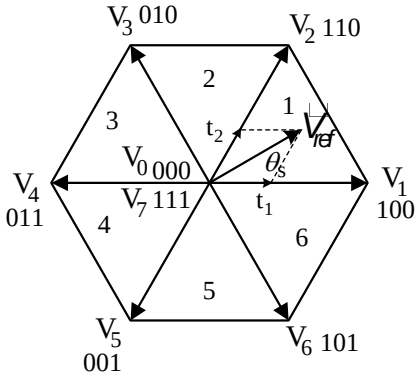

Fig. 5 Voltage space vector hexagon.

The hexagon is composed of 6 active vector (V1, …., V6) and 2 zero vector (V0 and V7). Six active vectors separate the hexagon into 6 sectors. The 2-zero vector are placed at the center of the hexagon. From Fig. 3, active voltage vector V1 has switching pattern as 100. The first digit "1" means the upper switch of phase A (S1) is turned on, while the lower switch of phase A (S4) is turned off. The second digit "0" means the upper switch of phase B (S3) is turned off, while the lower switch of phase B (S6) is turned on. The third digit "0" means the upper switch of phase C (S5) is turned off, while the lower switch of phase C (S2) is turned on. For other voltage vectors, the switching patterns are similar to V1.

The space vector (V_{ref}) rotates in the hexagon. At time t, the angle of the space vector refers to a-axis is θ_s, which is express as

$$\theta_s = \theta + \delta \tag{6}$$

At time t, the space vector (V_{ref}) can be at any sector 1 to sector 6. The number of the sector and the number of active vectors are determined by θ_s. If θ_s is between 0° and 60°, the space vector is in sector 1 and active vectors are V1 and V2. If θ_s is between 60° and 120°, the space vector is in sector 2 and active vectors are V2 and V3. If θ_s is between 120° and 180°, the space vector is in sector 3 and active vectors are V3 and V4. For other sectors, the active vectors and the number of the sector also can be found similar to this.

The times of each active vectors of a sector depend on the angle α, as represented in Fig 6.

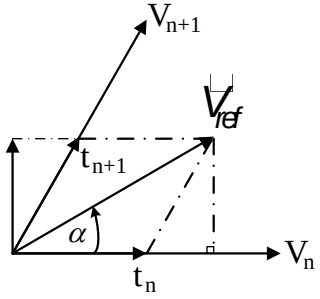

Fig. 6 Voltage space vector and adjacent active vectors.

Vn is the first active vector in sector n and Vn+1 is the second active vector in sector n. tn is a switching time of active vector Vn and tn+1 is a switching time of active vector Vn+1. From Fig.6, in a switching period (T), the average voltage of the space vector (V_{ref}) is defined as

$$\left|\vec{V}_{ref}\right| = \left|\vec{V}_n\right| \cdot \frac{t_n}{T} + \left|\vec{V}_{n+1}\right| \cdot \frac{t_{n+1}}{T} + \left|\vec{V}_z\right| \cdot \frac{t_z}{T} \tag{6}$$

where V_z is a zero vector and the magnitude of V_z is always zero. tz is switching time of the zero vector.

From Fig.6, the voltage equation can be written in a matrix form as,

$$T\left|\vec{V}_{ref}\right|\begin{bmatrix}\cos\alpha \\ \sin\alpha\end{bmatrix} = t_n \cdot \left|\vec{V}_n\right|\begin{bmatrix}1 \\ 0\end{bmatrix} + t_{n+1} \cdot \left|\vec{V}_{n+1}\right|\begin{bmatrix}\cos\frac{\pi}{3} \\ \sin\frac{\pi}{3}\end{bmatrix} \tag{7}$$

The magnitude of Vn and Vn+1 is defined as

$$\left|\vec{V}_n\right| = \left|\vec{V}_{n+1}\right| = \frac{2}{3}V_d \tag{8}$$

Thereby,

$$T\left|\vec{V}_{ref}\right|\begin{bmatrix}\cos\alpha \\ \sin\alpha\end{bmatrix} = t_n \cdot \frac{2}{3}V_d \cdot \begin{bmatrix}1 \\ 0\end{bmatrix} + t_{n+1} \cdot \frac{2}{3}V_d \cdot \begin{bmatrix}\cos\frac{\pi}{3} \\ \sin\frac{\pi}{3}\end{bmatrix} \tag{9}$$

when $0^\circ < \alpha \leq 60^\circ$

The switching time of active vectors Vn and Vn+1 can be expressed as

$$t_n = mT\sin\left(\frac{\pi}{3} - \alpha\right)$$
$$t_{n+1} = mT\sin\alpha \tag{10}$$

where m is a modulation index, which is given by

$$m = \sqrt{3}\frac{\left|\vec{V}_{ref}\right|}{V_d} \tag{11}$$

From equation (6), the switching time of zero vector is shown as follow

$$t_z = T - (t_n + t_{n+1}) \tag{12}$$

and $t_0 = t_7 = \frac{t_z}{2}$ when t0 and t7 is switching time of zero vectors V0 and V7 consecutively.

IV. SIMULATION AND RESULTS

The model of PMSM motor is created in MATLAB/Simulink to obtain the motor characteristics. The motor parameters in the simulation program are

Armature resistance	0.8 Ω/phase
Synchronous inductance	3.12 mH/phase
Pole pair	4
Back EMF constant	0.417 V/rad/s

The results of simulation are expressed in Fig. 7 to Fig. 10. Fig.7 shows the speed, torque, and phase current from SPWM by using modulation index (MI) at 0.68. Fig.8 illustrates the phase voltage and FFT analysis from SPWM at MI 0.68 and THD is obtained at 121.65%

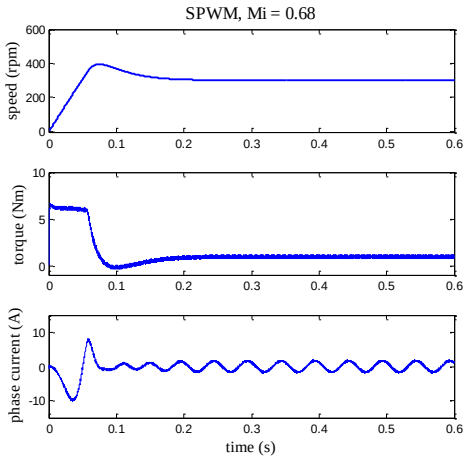

Fig. 7 Motor characteristics from SPWM at Mi 0.68.

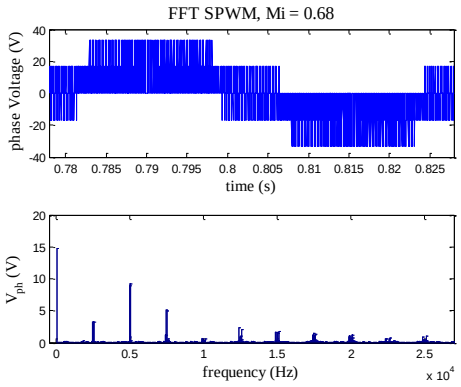

Fig. 8 Phase voltage and FFT analysis from SPWM at Mi 0.68.

To compare between SPWM and SVPWM modulation, the simulation from SVPWM are retrieved. The speed, torque, and phase current from SVPWM at MI 0.68 are illustrated in Fig.9. Fig.10 present the phase voltage and the FFT analysis from SVPWM at MI 0.68, of which THD is 92.09%.

To conclude and add more information about the motor characteristic at the same modulation index, Table1 present the motor torque, the peak voltage at the fundamental frequency and THD for 2 modulation indexes, 0.68 and 0.73.

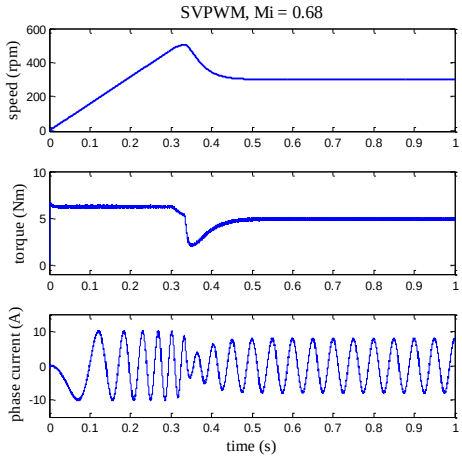

Fig. 9 Motor characteristics from SVPWM at Mi 0.68.

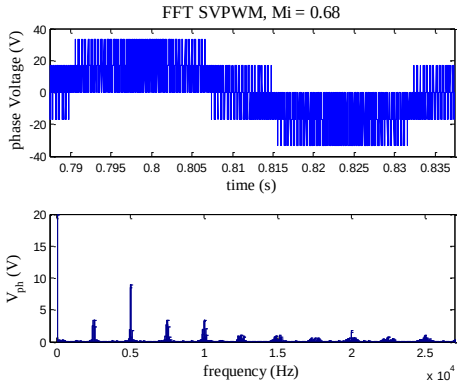

Fig. 10 Phase voltage and FFT analysis from SVPWM at Mi 0.68.

Table 1 Comparison motor characteristic between SPWM and SVPWM at the same modulation indexes.

Modulation		SPWM	SVPWM
Mi 0.68	Torque (Nm)	0.95	4.91
	Peak phase voltage (V)	14.78	19.87
	THD (%)	121.65	92.09
Mi 0.73	Torque (Nm)	1.17	5.97
	Peak phase voltage (V)	15.43	20.90
	THD (%)	114.21	87.04

It can be seen that THD from SVPWM are less than those from SVPWM by 30%. This shows the similar results as [3, 5]. From Table 1, torques from SVPWM are higher than those from SPWM by 80%. It is implied that if toques from SVPWM are higher than those from SPWM, the phase current and phase voltage from SVPWM are higher than those from SPWM. In general, to compare the performance of the motor, it is usually compared with the same motor torque and the same motor speed. Therefore, the motor characteristics from both modulations should also be compared with the same torque and the same speed.

Fig. 11(a) and (b) show the motor speed, torque, and phase current at the same torque at 4 Nm, and the same speed at 300 rpm, from SPWM and SVPWM, consecutively. The modulation index from SPWM is 0.8688 and that from SVPWM is 0.6393. It is clear that when using the same torque and the same motor speed, the modulation indexes from both modulation are different.

Fig. 12 (a) and (b) present the FFT analysis and the phase voltage from SPWM and SVPWM, successively. THD of the phase voltage from SPWM is 0.9990 and that from SVPWM is 1.0666. Two values are near though the THD from SVPWM is more than that from SPWM by 6.76%. The peak phase voltage at the fundamental frequency is also close, yet that from SPWM is slightly higher than that from SVPWM, as show in Table2.

Table 2 Comparison of motor characteristic from SPWM and SVPWM at the same torque and the same speed.

Modulation		SPWM	SVPWM
4 Nm	Modulation index	0.87	0.64
	Peak phase voltage (V)	18.40	18.00
	THD (%)	1.00	1.02
3 Nm	Modulation index	0.81	0.59
	Peak phase voltage (V)	17.43	17.19
	THD (%)	1.05	1.07

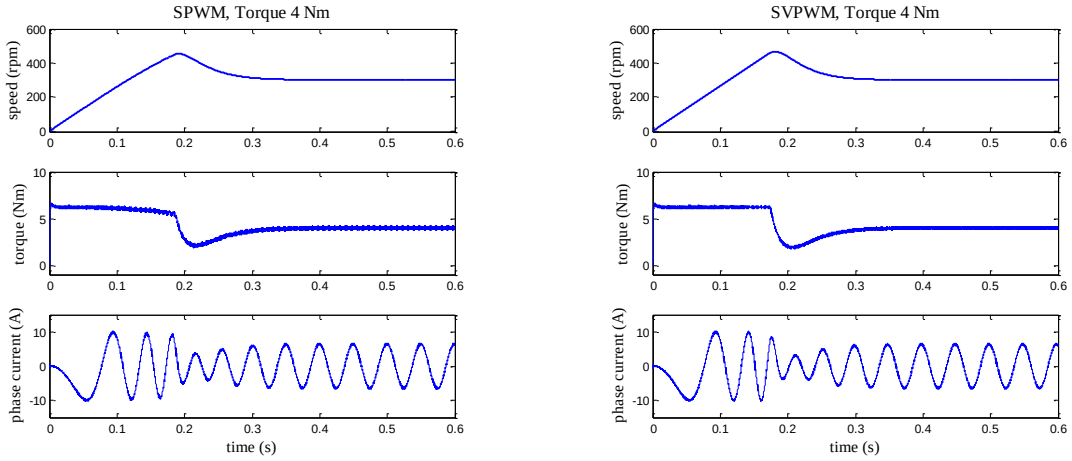

(a) (b)

Fig. 11 Motor characteristics at Torque 4 Nm (a) SPWM (b) SVPWM.

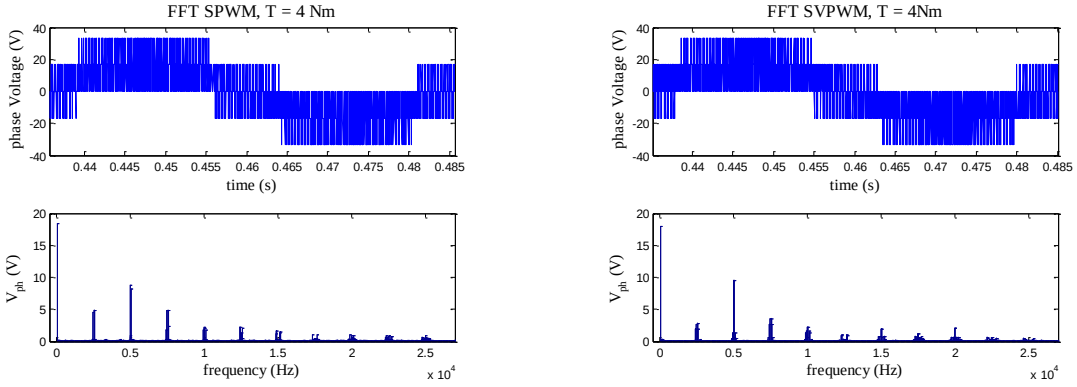

(b) (b)

Fig. 12 Phase voltage and FFT analysis at Torque 4 Nm (a) SPWM (b) SVPWM.

V. CONCLUSION

The simulation results of SPWM and SVPWM, which is carried out in MATLAB/Simulink, are shown. The motor characteristics, FFT analysis and THD, of both modulation approaches in the same modulation index and in the same motor torque are represented. Although the results from the same modulation index shows that THD from SVPWM is approximately 30% less than that from SPWM, the motor torque from SVPWM is greater than that from SPWM by 80%. On the other hand, the results from the same torque reveals that THD from SPWM is similar to that from SVPWM and the peak values of the phase voltage at the fundamental frequency from SPWM

is slightly higher than that from SVPWM. Hence the conclusion, that the SVPWM is better than the SPWM, is only true when the modulation index is equal. However, when using the same torque, it cannot be concluded like that.

REFERENCE

[1] B. Li and C. Wang, "Comparative analysis on PMSM control system based on SPWM and SVPWM," 2016 Chinese Control and Decision Conference (CCDC), Yinchuan, 2016, pp. 5071-5075.

[2] N. H. Saad, A. El Meged and A. M. A. Mahmoud, "Comparison of state space vector PWM schemes for a voltage source inverter," 2008 International Conference on Computer Engineering & Systems, Cairo, 2008, pp. 303-308.

[3] K. V. Kumar, P. A. Michael, J. P. John, and S. S. Kumar, "Simulation and Comparison of SPWM and SVPWM Control for Three Phase Inverter", ARPN Journal of Engineering and Applied Sciences, vol. 5, no. 7, pp. 61-74, 2010.

[4] D. Rathnakumar, J. LakshmanaPerumal and T. Srinivasan, "A new software implementation of space vector PWM," Proceedings. IEEE SoutheastCon, 2005., Ft. Lauderdale, FL, USA, 2005, pp. 131-136.

[5] R. H. Ahmad, G. G. Karady, T. D. Blake and P. Pinewski, "Comparison of space vector modulation techniques based on performance indexes and hardware implementation," Proceedings of the IECON'97 23rd International Conference on Industrial Electronics, Control, and Instrumentation (Cat. No.97CH36066), New Orleans, LA, USA, vol.2, pp. 682-687, 1997.

[6] L. Chengwu, Z. Xiaomin and J. Qiguang, "Research on SVPWM Inverter Output Control Technology," 2013 Fifth International Conference on Measuring Technology and Mechatronics Automation, Hong Kong, 2013, pp. 927-929.

[7] B. Hariram and N. S. Marimuthu, "Space vector switching patterns for different applications - a comparative analysis," 2005 IEEE International Conference on Industrial Technology, Hong Kong, 2005, pp. 1444-1449.

[8] B. Sujatha and K. Bhavya, "Simulation and Performance of AC Drives Using SVPWM Technique", International Journal on Recent and Innovation Trends in Computing and Communication, vol. 5, no. 7, pp. 11 - 18, Jul. 2017.

Analysis Design and Simulation of an Isolated Flyback-based Distributed Power Supply with Power Balance Control Technique

Jedsada Yodwong
Department of Electrical Engineering
Rajamangala University of Technology Lanna, RMUTL
Chiang Mai, Thailand
Jedsada_yodwong@hotmail.com

Uthen Kamnarn
Department of Electrical Engineering
Rajamangala University of Technology Lanna, RMUTL
Chiang Mai, Thailand
uthen@rmutl.ac.th

***Abstract*— The average small-signal analysis, and design of an isolated flyback-based distributed power supply based on power balance control technique is presented in this paper. The proposed procedure is simple and effective. The output voltage has good transient responses. The control circuit is simple and can be implemented by analog circuit.**

Keywords*— DC power supply; Converter control; Modeling; Simulation; Power balance control technique

I. INTRODUCTION

The connection structure of converters can be designed in a variety of connections, from 5 basic connections: Paralleling, Cascading, Source splitting, Load splitting, and Stacking. Which, when connecting the structures together, can conclude that all the structures can be connected to 9 structures which can be utilized in various situations. Form the following structure constructions, which are (1) Source splitting, (2) Source splitting and stacking output, (3) Source stacking, (4) Source stacking and paralleling output, (5) Source stacking and stacking output, (6) Source paralleling, (7) Source paralleling and paralleling output, (8) Source paralleling and stacking output, and (9) Cascading. When analyzed by connecting with 2 modules by using DC-DC Converters, can have many of connection patterns which have difference advantages, disadvantages, including limitations and solutions. Therefore, this analytical study can be used for a variety of converter extension formats up to infinity structures. This research will give examples of analysis, design and simulation of the connection structures in case of problems which are 2 boost converter circuits (a) stacking input and stacking output, and (b) Stacking input and paralleling output.

The desired converters should be small and have high power density, high efficiency, good responsiveness, and good robustness. High responsiveness and high robustness are required for the control systems of switching converters. Voltage Mode Control (VMC) and Current Mode Control (CMC) are the most basic control system of switching converters. However, it is difficult to improve the performance of boost-type DC-DC converters significantly using only this technology. This is because in boost-type DC-DC converters, the ON and OFF circuit states are different. As a result, the transfer function of any boost-type DC-DC converter includes an unstable zero (right half plane zero). Therefore, control systems based on boost-type DC-DC converters cannot set the gain-crossover frequency due to the presence of this unstable zero. Which, on the other hand, control of switching converter using sliding mode control (SMC) has been studied [1, 2]. Sliding mode control has high robustness and is resistant to influences by plant fluctuations. However, the control system has a problem that it is very complicated compared with VMC and CMC.

The control system design of the proposed system in this research begins with the analysis of the state-space average small-signal model of the system and simulates the model of the system in MATLAB Simulink Software. Then control the system using the Power Balance Control Technique method, which is simple in designing and resolving various limitations of the Voltage Mode Control and Current Mode Control. As a result, the performance of the control system can be greatly improved. Furthermore, the implementation is also very simple.

Fig. 1. shows the Boost converter circuit connection structures in case of problems. The analysis of the operation of the circuit can be done by considering the operation from the switching state in each period of time in which the system is operating in a stable state.

For Fig.1 (a), while in the state that the switch is in ON state (b). the current flows through both inductors and output capacitors instead of just flows through the inductors, which is incompatible with the converter operation. The current equation on the output side can be written as follows

$$i_{C1} = i_{C2} + i_{L2} - i_{L1} \qquad (1)$$

When the switch is in OFF state, the circuit has the current loop of i_{L2}, which produces loss and is incompatible with the converter operation. The current equation on the output side can be written as follows

$$i_{D1} = i_{C1} + i_{load} \qquad (2)$$

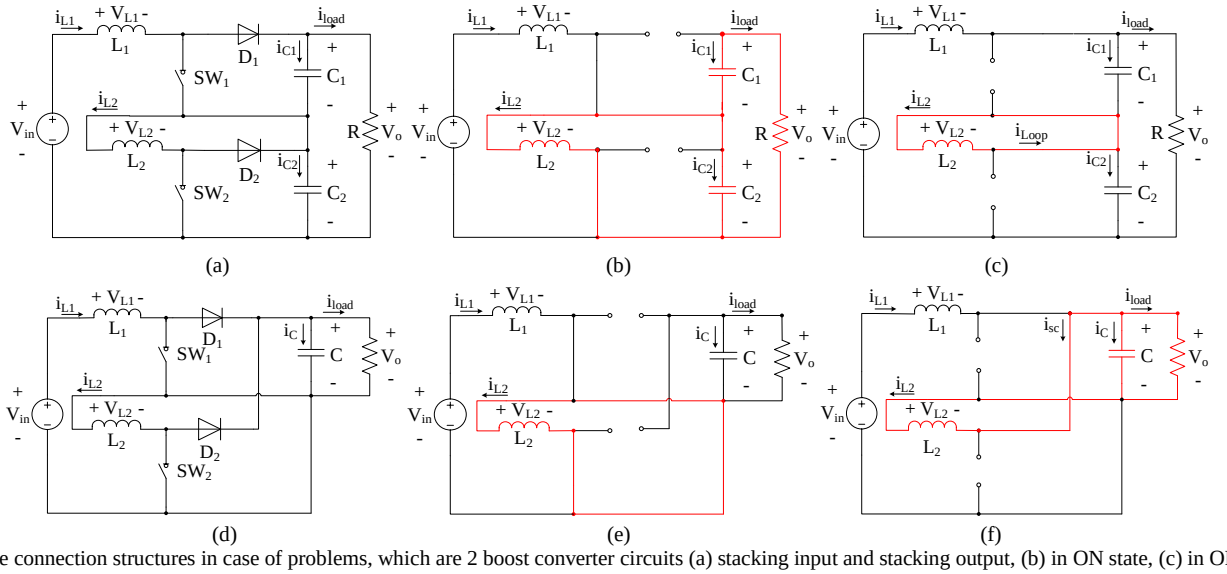

Fig. 1. The connection structures in case of problems, which are 2 boost converter circuits (a) stacking input and stacking output, (b) in ON state, (c) in OFF state. (d) Stacking input and paralleling output, (e) in ON state, (f) in OFF state.

$$i_{D1} = i_{C1} + i_{C2} \qquad (3)$$

For fig.1 (d), while in the state that the switch is in ON state (e). the current does not flow through inductor i_{L2} and only stored in i_{L3}. And when the switch is in OFF state (f), the current on the output side also flows through i_{L2} instead of just i_C and i_{load}, which is incompatible with the converter operation. The current equation on the output side can be written as follows

$$i_C = i_{L2} + i_{load} \qquad (4)$$

II. THE PROPOSED SYSTEM

The solution to the problem in the stacking input connection structure of boost converters can be solved by separating the circuit between the input and output side from electrically interconnected by using transformers to separate the circuits as follows. The purpose of a transformer is to transfer energy from the input winding to the output winding through electromagnetic induction. The minimal number of primary winding turns can be found from follows equation.

$$N_p = \frac{\lambda_m}{B_m A_C} \qquad (5)$$

Where, λ_m is maximum value of the flux linkage which should be calculated at maximum duty cycle given as

$$\lambda_m = V_p d T_s \qquad (6)$$

Where, A_C is the core cross section area, B_m is the saturation flux density of the core material, d is duty cycle, T_s is the switching period

The Power Balance Control technique for the proposed system is shown in Fig.2 (d). It shows a simple control block diagram which can be easily implemented by analog circuits. The proposed control technique consists of a proportional-plus-integral controller and inductor current calculator. The inductor current calculator computes the desired input current. The output voltage is measured and compared to the reference voltage. The voltage error is injected into and appropriate voltage controller. The summation signal is multiplied by a signal of rectified input voltage and compared to the input inductor current signal. The resulting signal is processed by a suitable hysteresis current control, generating signal to control the switch.

A. *Average Small Signal Analysis*

The analytical model derivation is based on the power stage schematic shown in Fig. 2 is based on a power balance control where the ideal switches and zero equivalent series resistance in the capacitors are assumed.

For Fig.2 (a),

$$I_L \cdot \sum_{i=1}^{N} V_{in_i} = I_{load} \cdot \sum_{i=1}^{M} V_{C_i} \qquad (7)$$

For Fig.2 (b) and (c),

$$I_L \cdot \sum_{i=1}^{N} V_{in_i} = V_o \cdot \sum_{i=1}^{M} I_{load_i} \qquad (8)$$

For Fig.2 (d),

$$V_{in} \cdot \sum_{i=1}^{N} I_{L_i} = V_o \cdot \sum_{i=1}^{M} I_{load_i} \qquad (9)$$

When, V_{in} is the DC input voltage, I_L is the inductor current, V_o is the output voltage, V_C is the capacitor voltage, I_{load} is the load current, N is number of converters in the system.

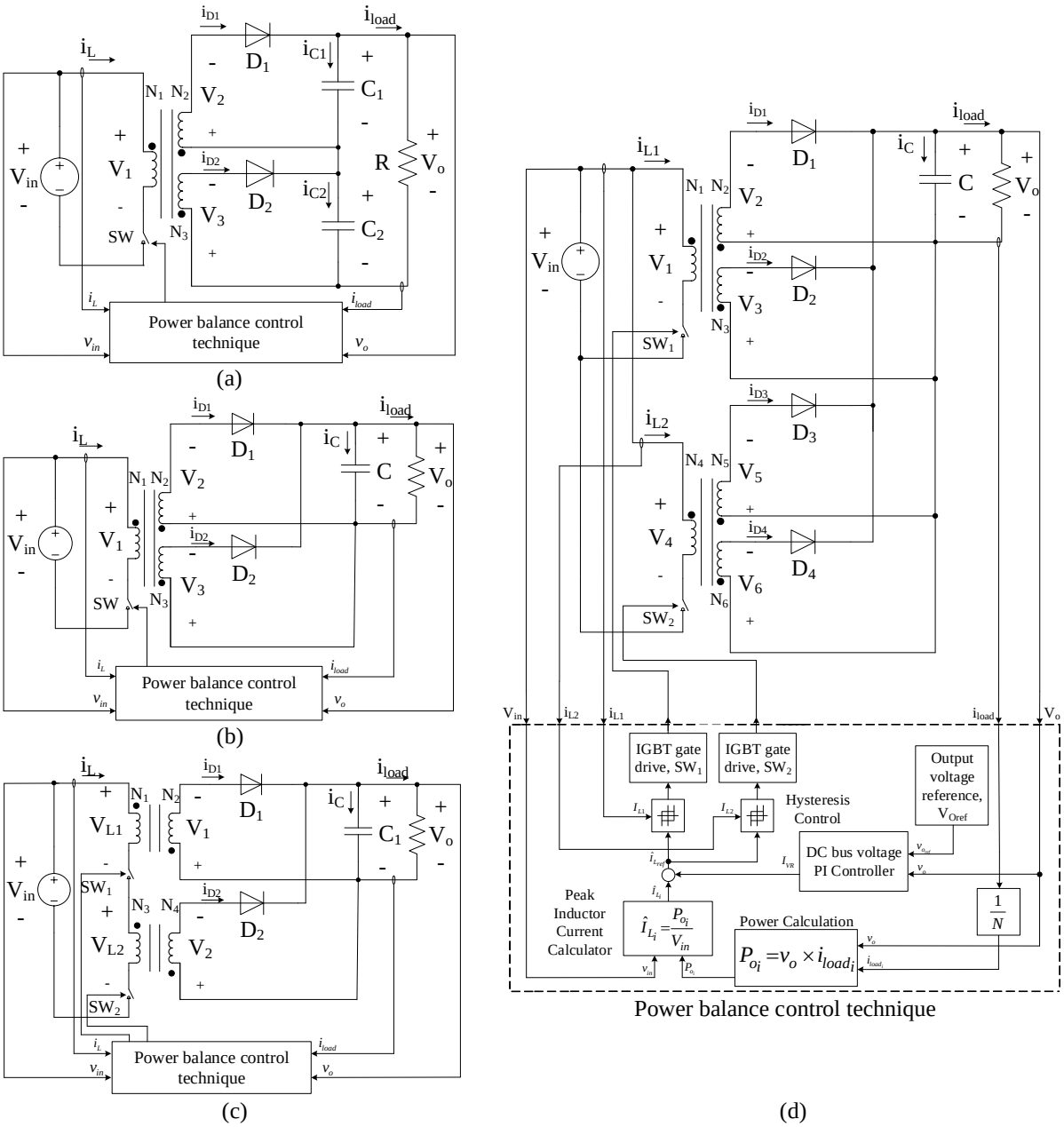

Fig. 2. The circuit used to solve the problems of the stacking input connection structure of boost converters, which are (a) stacked output flyback converter with 1 transformer, (b) paralleled output flyback converter with 1 transformer, (c) paralleled output flyback converter with 2 transformers, (d) paralleled 2 module flyback converters with paralleling output. With Power balance control technique.

The peak value of the inductor current is

$$\hat{I}_{Lref_i} = \hat{I}_{L_i} + I_{VR} \qquad (10)$$

$\hat{I}_{L_i}$ is the value of the inductor current, $\hat{I}_{Lref_i}$ is peak value of the inductor reference current, I_{VR} is correcting signal of PI controller.

The dynamic equation of the output voltage is

$$\sum_{i=1}^{N} I_{oi} = I_o = C_o \frac{dV_o}{dt} + I_{load} \qquad (11)$$

Applying the perturbations in (7) to (11) and performing the small-signal approximation. Therefore, the output voltage can be expressed as follows

For Fig.2 (a),

$$\frac{\tilde{v}_o}{\tilde{v}_{ref}} = \frac{G_{VR} \cdot \sum_{i=1}^{N} \bar{V}_{in_i}}{C(S) \cdot \sum_{i=1}^{M} \bar{V}_{C_i} + k_{fb} G_{VR} \cdot \sum_{i=1}^{N} \bar{V}_{in_i}} \qquad (12)$$

For Fig.2 (b) and (c),

$$\frac{\tilde{v}_o}{\tilde{v}_{ref}} = \frac{G_{VR} \cdot \sum_{i=1}^{N} \bar{V}_{in_i}}{\bar{V}_o C(S) + k_{fb} G_{VR} \cdot \sum_{i=1}^{N} \bar{V}_{in_i}} \qquad (13)$$

For Fig.2 (d),

$$\frac{\tilde{v}_o}{\tilde{v}_{ref}} = \frac{G_{VR} \bar{V}_{in_i}}{\bar{V}_o C(S) + k_{fb} G_{VR} \cdot \sum_{i=1}^{N} \bar{V}_{in_i}} \qquad (14)$$

That is, the output voltage of the converters is independent of variations in the load current. The voltage regulator G_{VR} must be chosen so as to minimize the influence of the audio susceptibility and the output impedance, while the steady-state error of the output voltage should also be small as possible.
The PI controller is chosen for voltage regulation is

$$G_{VR}(s) = \frac{k_p (S + \omega_Z)}{S} \qquad (15)$$

When, k_{fb} is the feedback gain, $G_{VR}(s)$ is PI controller, k_p is the gain of controller, ω_Z is the location of the zero.

It is convenient to use the loop gain for analyzing the stability of the closed-loop system. The frequency response analysis is used to describe the stability of the proposed system. The design of the output voltage control loop must guarantee the stability and provide enough bandwidth in all the possible operation conditions of the system.

III. Simulation Results

The simulation results of the proposed systems are shown in Fig. 3 to Fig. 8 The transient respond effectiveness of the systems are examined by computer simulation in MATLAB Simulink using the specification shown in the table I. The proposed of this simulation is to verify the control algorithms, design the controller parameters, and study the static and dynamic performance of the proposed system.

Table I. Design results

Parameter	Value			
	The paralleled output flyback converter with 1 transformer	***The stacked output flyback converter with 1 transformer***	***The paralleled output flyback converter with 2 transformers***	***The paralleled 2 module flyback converters with paralleling output***
Transformer magnetizing inductance	31 µH	62 µH	13 µH	31 µH
Transformer turns ratio	1:2:2	1:2:2	1:2, 1:2	1:2:2, 1:2:2
Output capacitance, C_O	96 µF	48 µF, 48 µF	232 µF	384 µF
Output voltage ripple, $\Delta V_o/V_o$	1 %	1 %	1 %	1 %
Input voltage, V_{in}	12 V	12 V	12 V	12 V
Switching frequency	25 kHz	25 kHz	25 kHz	25 kHz
Total output power	72 W	72 W	72 W	288 W
Output voltage	30 V	60 V	30 V	30 V

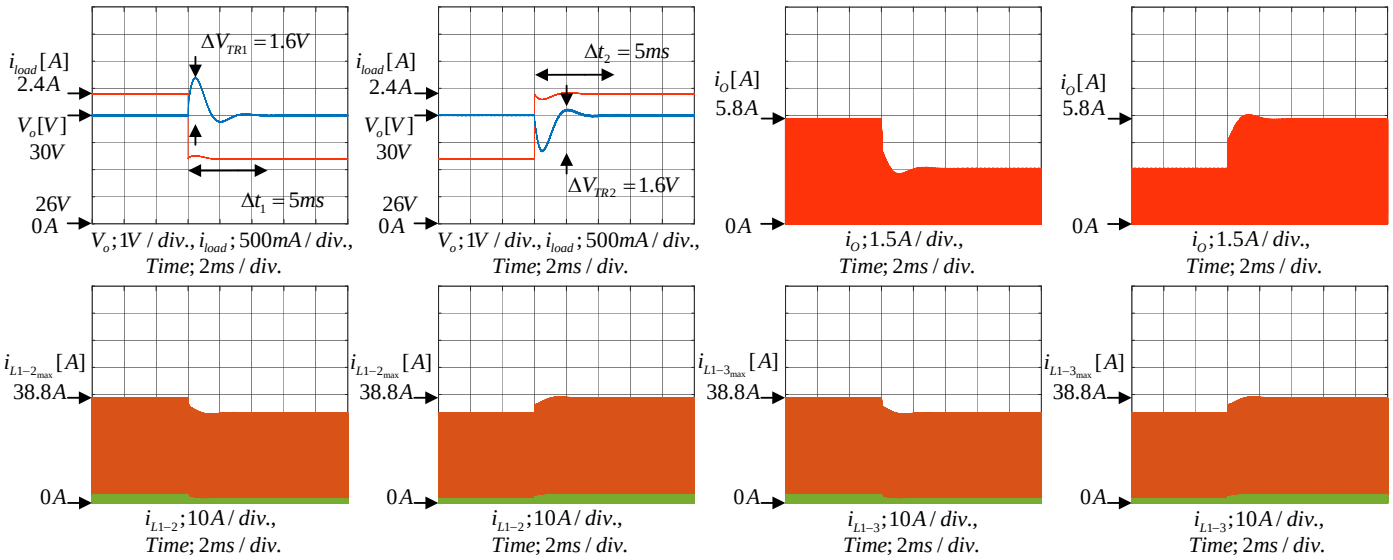

Fig. 3. Transient condition of (b) the paralleled output flyback converter with 1 transformer. At step load change from 100% to 50% and vice versa (parameter of PI controller k_p = 1.3 and ω_Z = 7000).

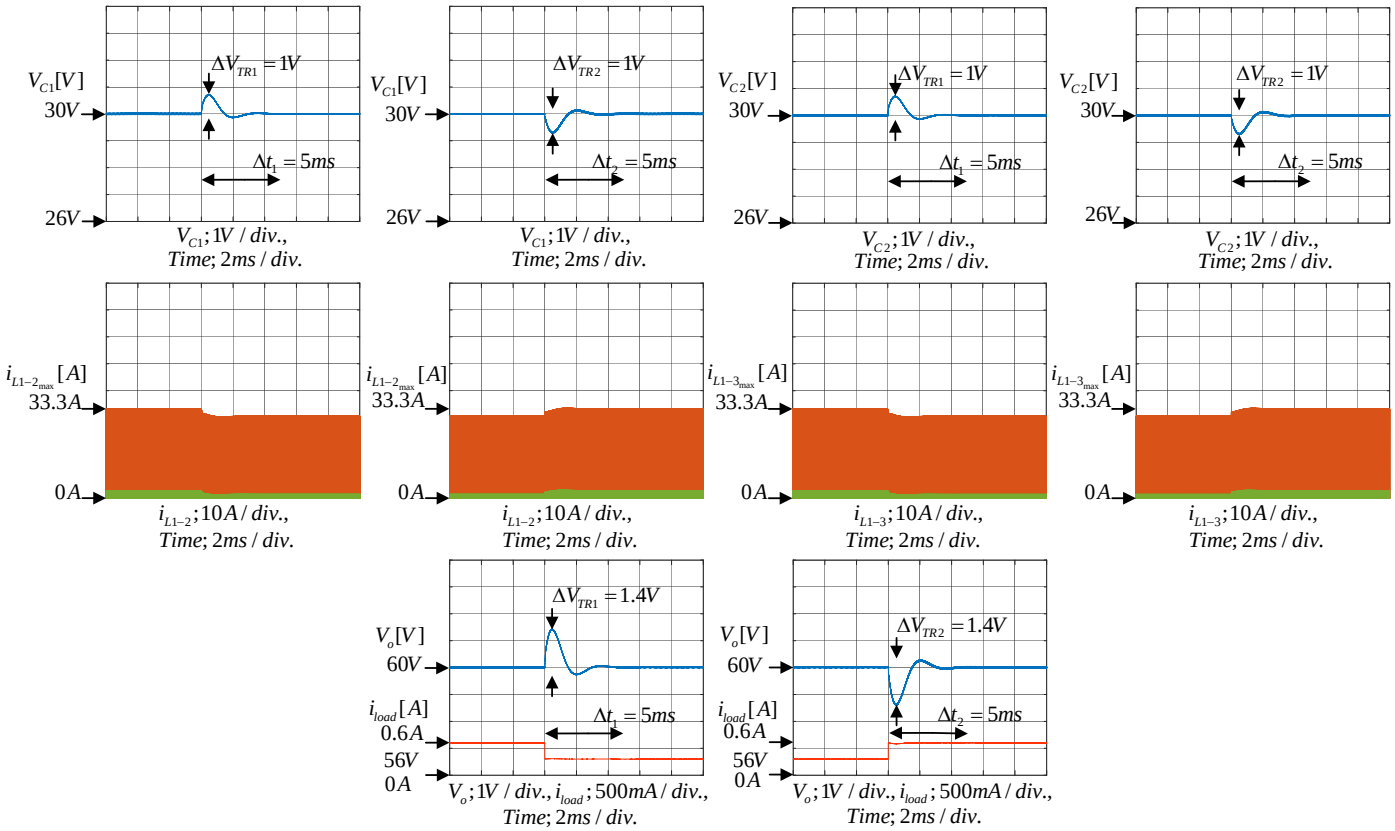

Fig. 4. Transient condition of (a) the stacked output flyback converter with 1 transformer. At step load change from 100% to 50% and vice versa (parameter of PI controller k_p = 1.3 and ω_Z = 7000).

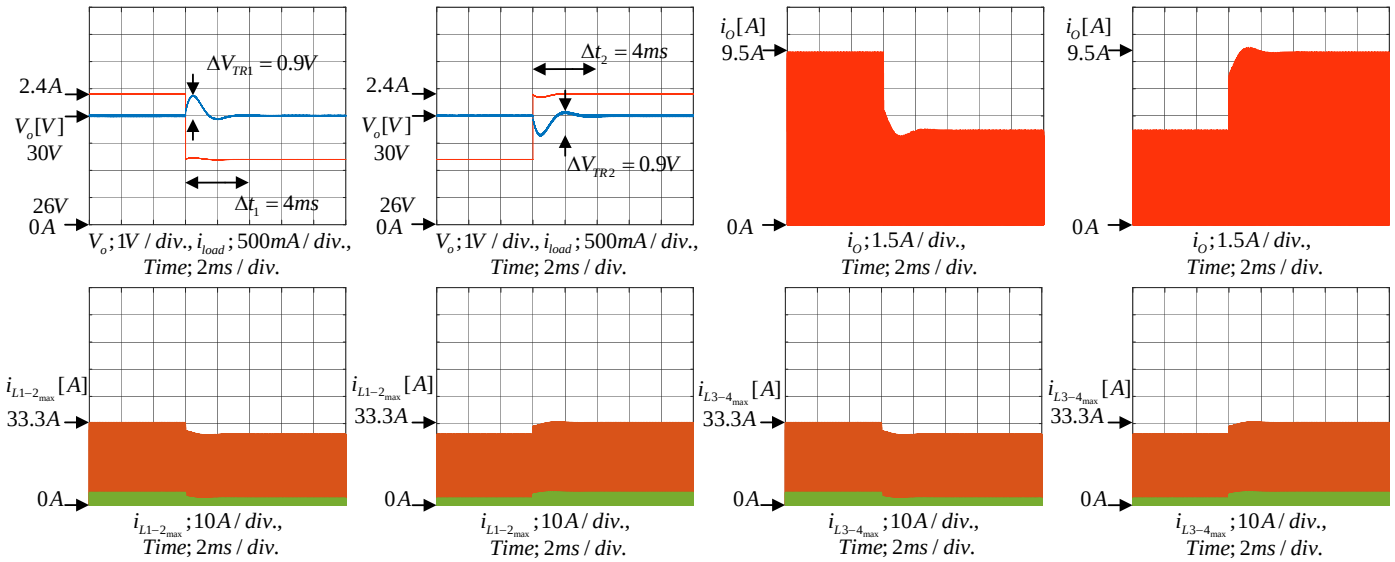

Fig. 5. Transient condition of (c) the paralleled output flyback converter with 2 transformers. At step load change from 100% to 50% and vice versa (parameter of PI controller k_p = 1.3 and ω_Z = 7000).

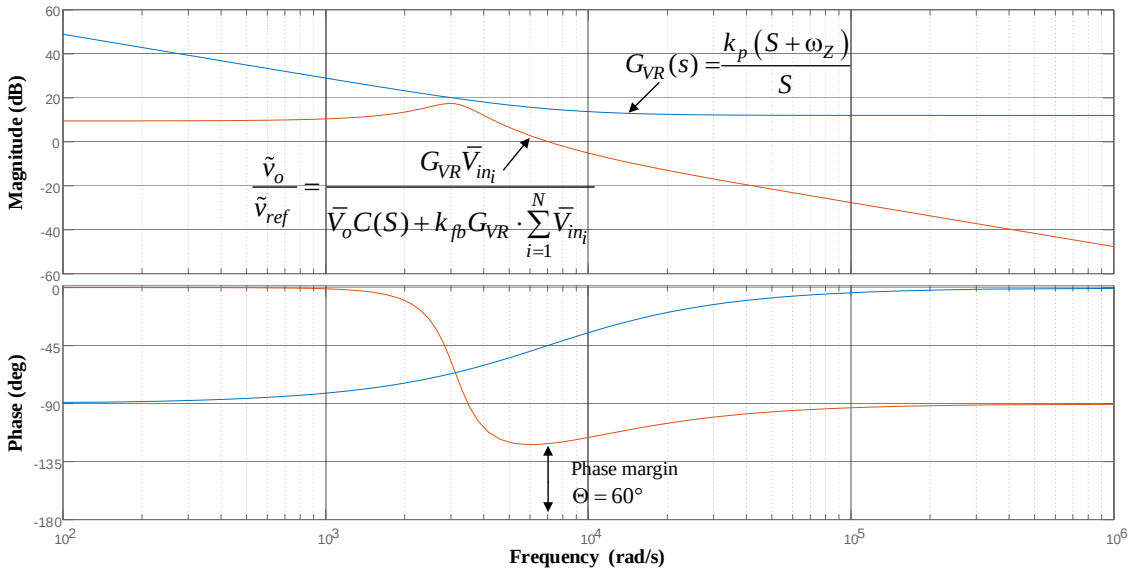

Fig. 6. Representative Bode plots of (d) the paralleled 2 module flyback converters with paralleling output.

Fig. 7. Simulation result for the output voltage V_o, load current i_{load}, the diode currents for symmetric mains condition (i_{D1}, i_{D2}, i_{D3}, i_{D4}), module loss in 1 and 2, and steps load change from 100% to 50% and back to 100%

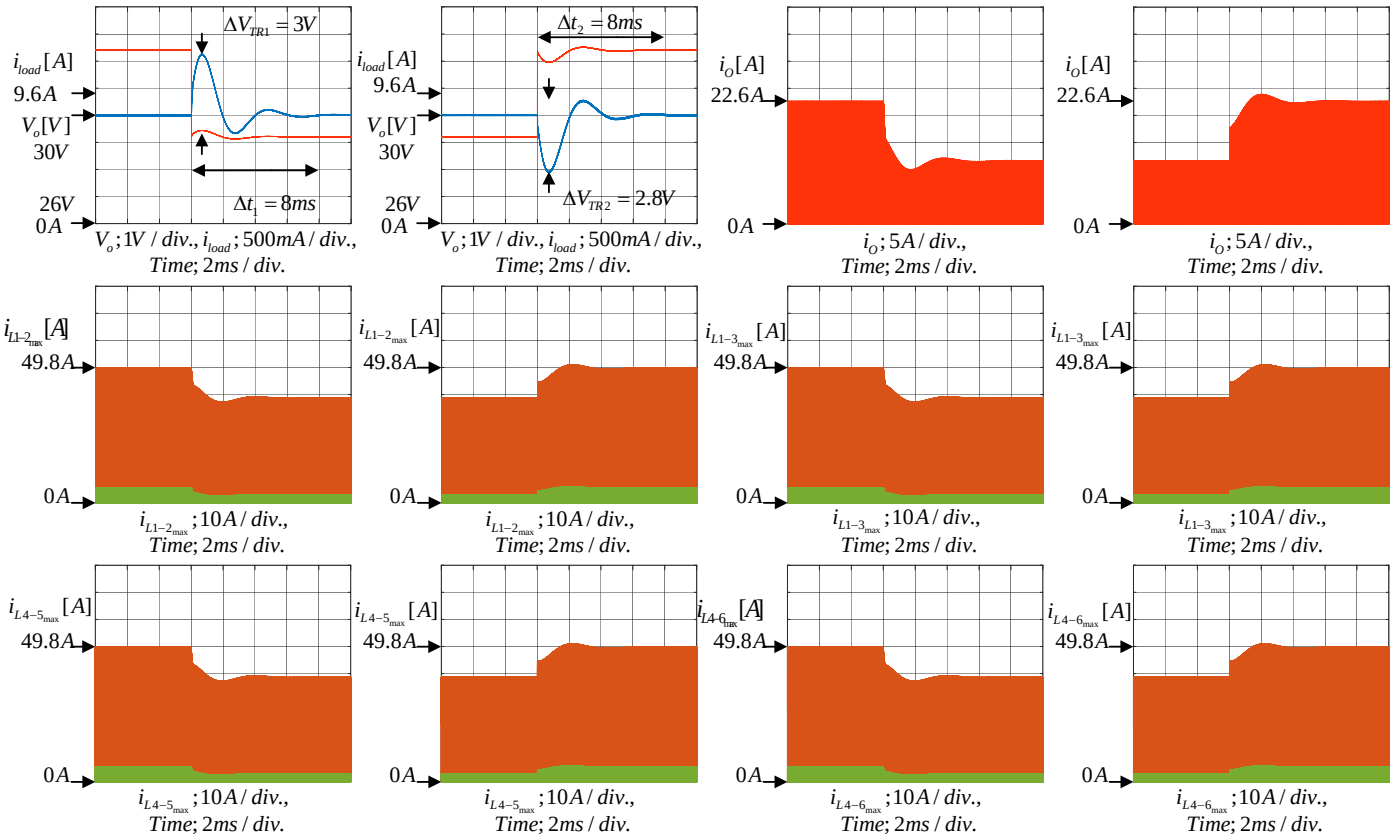

Fig. 8. Transient condition of (d) the paralleled 2 module flyback converters with paralleling output. At step load change from 100% to 50% and vice versa (parameter of PI controller k_p = 1.3 and ω_Z = 7000).

IV. Conclusion

The average small-signal analysis, and design of an isolated flyback-based distributed power supply based on power balance control technique has been presented in this paper. The main advantages are to troubleshoot the proposed system problems, limitations, and improve dynamic response. The proposed procedure of analysis is simple and effective to derive the system models, including the inductor current loop and voltage loop. The average small-signal model of the voltage loop leads to the key point of designing the inductor current compensator. The input current of the converter module was controlled by the hysteresis control circuit. According to the results obtained, the output voltage is regulated to have good transient responses by the designed PI controller with power balance control technique, the purposed system provides good inductor current sharing among the converter modules and the control circuit is simple and can be implemented by analog circuit.

References

[1] Hongmei Li and Xiao Ye, "Sliding-mode PID control of DC-DC converter," 2010 5th IEEE Conference on Industrial Electronics and Applications, Taichung, 2010, pp. 730-734.

[2] D. Seshachalam, R. K. Tripathi and D. Chandra, "Practical Implementation of Sliding Mode Control for Boost Converter," APCCAS 2006 - 2006 IEEE Asia Pacific Conference on Circuits and Systems, Singapore, 2006, pp. 650-653.

[3] V. Chunkag and U. Kamnarn, "Parallelling three-phase AC to DC converter using CUK rectifier modules based on power balance control technique," in IET Power Electronics, vol. 3, no. 4, pp. 511-524, July 2010.

[4] A. Hassanzadeh, M. Monfared, S. Golestan and R. Dowlatabadi, "Small signal averaged model of DC choppers for control studies," Proceedings of the 2011 International Conference on Electrical Engineering and Informatics, Bandung, 2011, pp. 1-4.

[5] S. Gangavarapu and A. K. Rathore, "A Three-Phase Single-Stage Isolated Flyback-based PFC Converter with Leakage Energy Recovery Clamping circuit," in IEEE Transactions on Transportation Electrification.

Design of the Hybrid System for Voltage Control to the AC Load

Nattapong Phanthuna, Akaradage Khongkapong and Panisra Phrmmanok
Faculty of Engineering
Rajamangala University of Technology Phra Nakhon
Bangkok Thailand.
Nattapong.p@rmutp.ac.th

Siddaraj Uppin
Department of Electrical and Electronics Engineering
Manipal Institute of Technology
Karnataka India
Siddaraj.u@manipal.edu

***Abstract*— In this research has proposed the designing elements of hybrid system in order to transfer electrical power effectively to an AC load from the renewable energy sources and analysis with improved the result of transmission power, which the researcher had studied the photovoltaic (PV) system, fuel cell stack, models of DC to DC converter (Step up) and internal controller, models of the DC to AC converter and control system and design of a LC filter. The energy sources of this paper have used PV and fuel cells, while the step up converter (Boost converter), It has responsibility for increasing the voltage to the inverter system in order that convert the DC to AC current and adjust the voltage at modulation index value, after that will adapt the signal on LC filter for transferring that power to the AC load. The above has been presented and analyzed in this paper from the MATLAB/Simulink Program, which shown this hybrid system could efficiently transfer power as requirements of the load. Moreover, this paper can also use as a model for creating renewable systems by using power electronic devices and the future can expand this system to a larger for responding as load demand**

Keywords—Hybrid System, Boost Converter, Fuel cell, PV

I. INTRODUCTION

Electrical energy is an important factor in the being of humans and living organisms, but most electricity sources or power plants are using oil, petroleum, fuel, and coal to produce electricity, which in the future that must have a chance to disappear because those fuels has limited energy [1-3]. Therefore, need search a new existing energy sources or renewable energy sources, the PV and fuel cells are another alternative energy that has been introduced because those sources are renewable and clean energy without pollution [4,5].But the transmission system needs to add power converters or conversion systems and filter circuit for transmitting that power to an AC load. In this paper, using power converters because that converter can adjust voltages as load required and able to connect very well with both the PV and fuel cells. All of the power converters within the hybrid system consisted of two DC to DC converters and a DC to AC converter (inverter). Moreover, that hybrid system has the internal controllers and LC filter, which in this paper has studied the design principles and work theories with the objectives as follows:

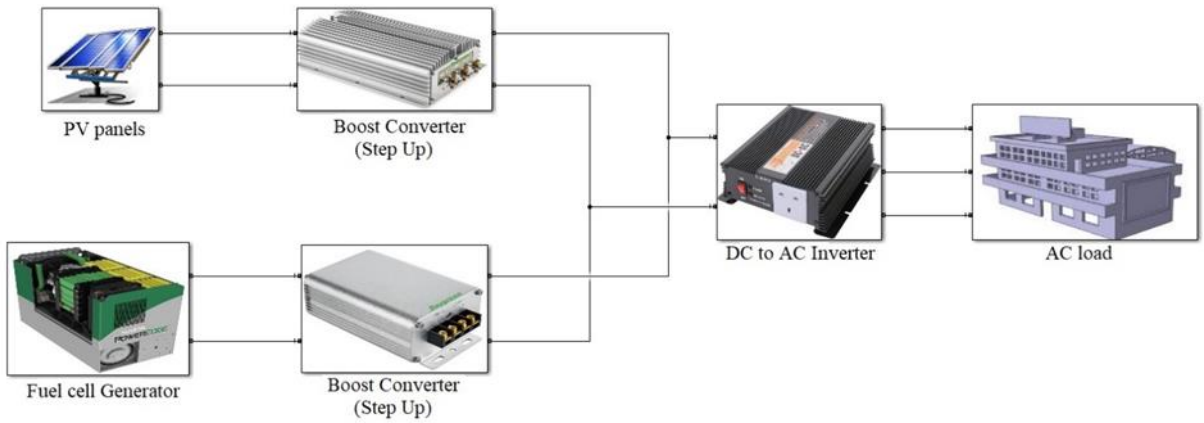

Fig. 1. Main block diagram of the hybrid system

- To use efficiently energy from photovoltaic (PV) and fuel cells
- To designs of the circuit and control system within a hybrid system
- Transfer the electric power effectively
- Quality and continuity of energy product.
- Analysis and improved the transmission power of a hybrid system for sending energy to the AC

II. THE PROPOSED DESIGN FOR MODELING THE HYBRID SYSTEM

The main block diagram of the proposed hybrid system features the PV panel, fuel cell stack, DC to DC converter (Step up) for a PV system, DC to DC converter (Step up) for fuel cell stack and DC to AC inverter with three-phase load is presented in Fig. 1. The elements in the block are connected by having the both systems (PV and fuel cells) are energy sources for sending voltage to the DC to DC converter. And then that converter will increase the electrical voltage in transmitting the energy to the DC to AC inverter system in order to convert the DC current to AC current which then transferring to AC load through an LC filter circuit within the inverter system. Which will present all of design theory for modeling the hybrid system as these topics below.

III. PHOTOVOLTAIC (PV) SYSTEM

The main parameters are used to describe PV capability consisting of the short-circuit current density (I_{sc}) and the open circuit voltage (V_{oc}). Which the short circuit will happen when the both terminals are directly connected with each other be the cause of the current is maximum and the voltage is zero [6,7]. For the terminal cases are not connected to load, the voltage in PV will be increased to maximum voltage, but there will be no flowing current which is called "open circuit voltage". The equivalent circuit of a typical PV is shown in the Fig. 2, by the shunt resistance (R_{sh}) is responsible to take the leakage current to the ground when the diode is in reverse biased, the series resistance (R_s) will take to consider the voltage drops and internal losses due to the flow of current. That can into account different PV properties from these equations below (1-2).

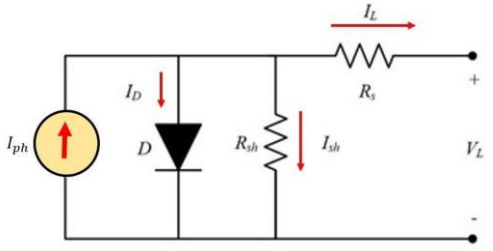

Fig. 2. Equivalent circuit of a typical PV

$$I = I_{ph} - I_D - I_{sh} \quad (1)$$

$$I = I_{ph} - I_o.\left(\exp\frac{(V_o+I.R_s)}{(n.V_T)} - 1\right) - \frac{V_o+I.R_s}{R_{sh}} \quad (2)$$

where

I_{sh}	=	Shunt current (A)
I_L or I	=	Output current (A)
I_{ph}	=	Photocurrent (A)
I_D	=	Diode Current (A)
I_{sat}	=	Diode reverses saturation current (A)
V_L or V_o	=	Output Voltage (V)
R_s	=	Series resistance
R_{sh}	=	Shunt resistance (Representing leakage currents)
k	=	Boltzmann constant, 1.3865×10^{-23} J/K
q	=	Charge on electron, 1.6021×10^{-19} C
N_s	=	Number of cells in series
n	=	Diode ideality factor
T_{cell}	=	Solar panel temperature
V_T	=	thermal voltage equivalent (At 25°C, $V_T \approx 0.0259$ V)
I_{sc}	=	Short Circuit Current
V_{oc}	=	Open Circuit Voltage

In order to a higher power can be obtained by making series and parallel of PV connection. The series connection is done to increase the output voltage such as PV connection, the individual panel voltages will add together, but the amperage must be limited to the value of the lower panel in the series string as shown in Fig. (3). The parallel connection has objective as same as series connection, but will change from increasing voltage to current as in case parallel PV connection the amperages are combined, while the voltage will adjust to the lowest value of connection [11,12] as shown in Fig. (4). In this research had the series connection 14 points and parallel connection 15 points for getting the electric real power to be 50 kW, by the parameters of a PV are 250.263W, 29.9V and 8.37A

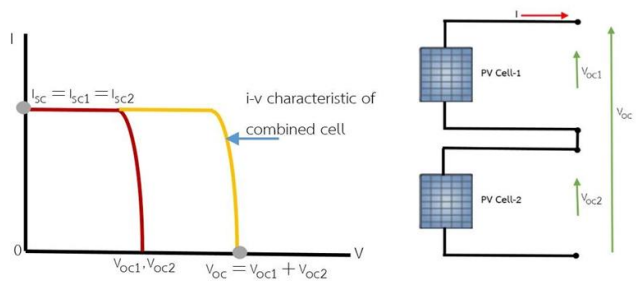

Fig. 3. *I-V characteristic of series PV connection*

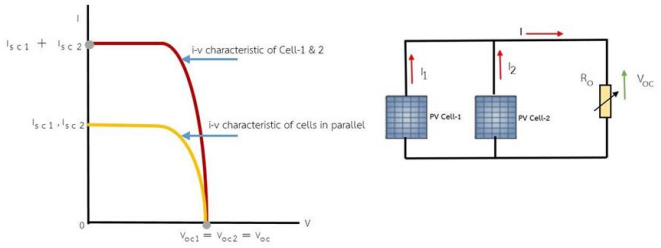

Fig. 4. *I-V characteristic of parallel PV connection*

IV. FUEL CELL STACK

Before you begin to format your paper, first write and save the content as a separate text file. Keep your text and graphic files separate until after the text has been formatted A fuel cell is a device that generates electricity by reacting between hydrogen and oxygen (obtained from air) which has three main working principles to create the chemical reaction. First, the oxygen enters the cathode layer, while hydrogen is fed to the anode of electrons for becoming to a positive charge. Second, the electrolyte will be transferring ionized hydrogen atoms from the anode to the cathode. Third the oxygen will combine with electrons for returning the ionized hydrogen atoms [13]. Moreover, the chemical reactions inside the fuel cell are as follows:

$$H_2 + \frac{1}{2}O_2 \rightarrow H_2O + \text{electrical energy} + \text{heat} \quad (3)$$

Typically, the fuel cell output voltage V_{cell} is defined by Ref

$$V_{cell} = E - V_{act} - V_{ohm} - V_{conc} \quad (4)$$

E is the Nernst voltage in terms of gas molarities, V_{act} is the over-voltage due to activation resistance and the ohmic over voltage is called V_{ohm}. Besides, V_{conc} is the concentration over voltage. For the fuel cell parameters of this research are 625V and 50kW.

V. MODELS OF DC TO DC CONVERTER (STEP UP) AND INTERNAL CONTROLLER

A boost converter is a DC-DC converter that provides an output voltage greater than the source voltage. The circuit diagram of a boost converter is shown in Fig. (5). The output voltage of the boost converter depends on the duty cycle for controlling the switch. Thus, the duty cycle (D) of this converter can be calculated using equation (5). Where V_{in} and V_o are the input and output voltages of the converter. The output power of the converter is equal to input power in equations (6.1-6.2), which the design of inductor and capacitor values within boost converter is calculated using as equations (7) and (8)

$$D = 1 - \frac{V_{in}}{V_o} \quad (5)$$

$$P_o = P_{in} = \frac{V_o^2}{R} \quad (6.1)$$

$$P_o = P_{in} = I_o V_o \quad (6.2)$$

$$L = \frac{V_{in} D}{f_s \Delta I_L} \quad (7)$$

$$C = \frac{I_o D}{f_s \Delta V_o} \quad (8)$$

Where f_s is the switching frequency and ΔI_L is the input current ripple. Current ripple factor is the ratio between input current ripple and output current. In good estimate of inductor value in current ripple factor should bound within 30% and $\Delta V_o$is the output voltage ripple which is usually considered as 5% of output voltage which yields as shown in the below equations (9) and (10).

$$\frac{\Delta I_L}{I_o} = 0.3 \quad (9)$$

$$\frac{\Delta V_o}{V_o} = 0.05 \quad (10)$$

In the practical case of boost converter, we can design the series resistance with an inductor value (R_L) and series resistance with a capacitor value (R_c) are calculated using the equations (11), (12) and (13).

$$I_{L,MAX} = \frac{V_o I_o}{V_{in}} + \frac{\Delta I_L}{2} \quad (11)$$

$$\frac{\Delta V_o}{I_{L,MAX}} = R_c \quad (12)$$

$$V_o = \left(\frac{V_{in}}{1-D}\right)\left(\frac{1}{1+\frac{R_L}{R(1-D)^2}}\right) \quad (13)$$

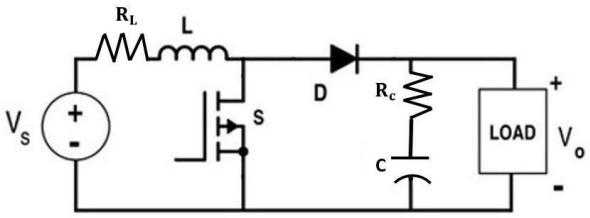

Fig. 5. Practical circuit of a Boost Converter

A. *Design of Boost converter for PV system*

The design of boost converter, we must know the Initial voltage of PV system. In this case the base PV voltage is 418.6V which needs to increase the voltage to 800V because of this case the inverter system will be converting the DC to AC current that has the output voltage provides AC load is around 400V.By designing the boost converter system can calculate from equations (6)-(13). So, all of parameters within this boost converter for PV system are shown in table 1.

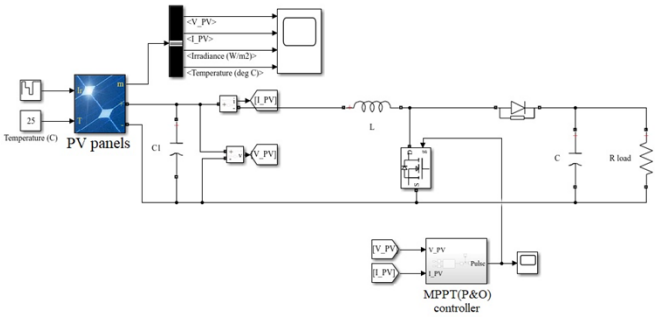

Fig. 6. A boost converter circuit of PV source within hybrid system

TABLE I. PARAMETERS OF THE BOOST CONVERTER FOR SOLAR CELLS (PV) SYSTEM

Duty cycle of the control switch.	D	0.477 or 47.7%
Input Voltage	V_{in}	418.6 V
Output Voltage	V_o	800 V
Output Power	P_o	50 kW
Input Power	P_{in}	50 kW
Output Current.	I_o	62.5 A
Input current ripple.	ΔI_L	18.75 A
Switching Frequency	f_s	10 kHz
Inductor value of the Boost.	L	$1.0649e^{-3}$ H
Capacitor value of the Boost.	C	$74.53125e^{-6}$ F
Output voltage ripple	ΔV_o	40 V
Load resistance.	R	12.8 ohm
Resistance capacitor.	R_c	0.3105 ohm
Resistance inductor.	R_L	0.0018 ohm

B. *MPPT Controller of Boost Con*

The MPPT method is an automation controller that finds the current maximum power point (IMPP) or voltage maximum power point (VMPP), by working to extract the maximum output power (MPP) of irradiance and temperature. Moreover, most widely used MPPT algorithms, they are 1. Perturb and Observe (P&O) 2. Incremental Conductance (IC) [14,15]. In this case we chose P&O because is a detector the operation point of increased power direction, by sensing voltage or current within PV panel. Therefore, if the power expands according the voltage, that power is sensed again until zero, which has the working principle flow chart of P&O and the input values are 50kW, 418.6V and duty cycle is 47.7%. According in Fig 7.

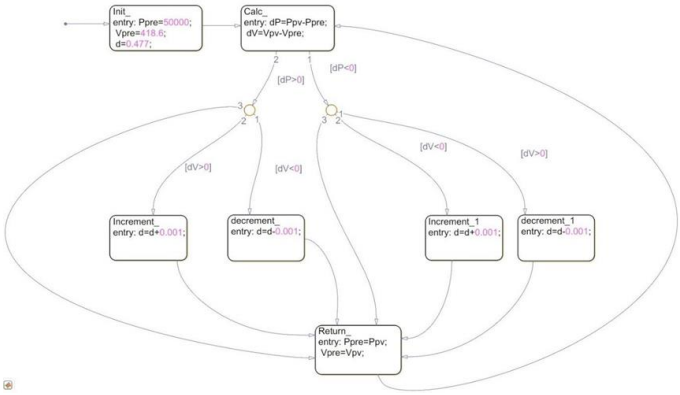

Fig. 7. Working Principle flow chart direction of Perturb and Observe (P&O) in MATLAB simulink program

C. *Designs of boost converter and control system for fuel cell*

The designing principle of this boost converter is similar as the PV system, but in this case the control system will be changed to a closed loop control system that can design a controller to generate duty cycle correction such that the output voltage is maintained constant. In this regard, we can be written the transfer function in terms of the converter parameter [16] as equation (14). Wherewith, the fuel cell can produce the input voltage is 625 V, the switching frequency is 25 kHz, the output values are V_o = 800V and $P_o = P_{in} = 50kW$. Therefore, all of these parameters in the boost converter can be calculated from equations 1-10 as same as the PV system by having those parameter shows in table II.

$$\frac{\tilde{v}_o(s)}{\tilde{d}(s)} = \frac{(1-D).V_o-(LI_L)s}{(LC)s^2+\frac{L}{R}s+(1-D)^2} \quad (14)$$

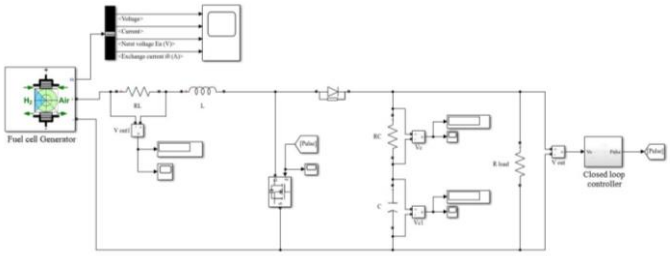

Fig. 8. A boost converter circuit of fuel cell source within hybrid system

TABLE II. PARAMETERS OF THE BOOST CONVERTER FOR FUEL CELLS SYSTEM

Duty cycle of the control switch.	D	0.22 or 22%
Input Voltage	V_{in}	625 V
Output Voltage	V_o	800 V
Output Current.	I_o	62.5 A
Output Power	P_o	50 kW
Input Power	P_{in}	50 kW
Input current ripple.	ΔI_L	18.75 A
Inductor value of the Boost.	L	$293.33e^{-6}$ H
Output voltage ripple	ΔV_o	40 V
Switching Frequency	f_s	25 kHz
Output voltage ripple	ΔV_o	40 V
Capacitor value of the Boost.	C	$13.75e^{-6}$ F
Load resistance.	R	12.8 ohm
Output current maximum	I_{LMAX}	89.375 A
Resistance capacitor.	R_c	0.4475 ohm
Resistance inductor.	R_L	0.0016 ohm

VI. MODELS OF DC TO AC CONVERTER AND CONTROL SYSTEM

The DC to AC converter is used to convert the DC voltage into a constant AC supply at constant frequency. But the converting current of inverter need to have the controller or control system for transmitting the voltage. In this research used the two-level space vector pulse width modulation (SVPWM) to be a generator for sending the control signal to three- phase inverter. According in Fig 10. The working principle of the SVPWM is a special switching sequence of the upper three power transistors of a three-phase power inverter which generate less harmonic distortion in the output voltages and currents applied to the phases of an AC motor [17].

VII. DESIGN OF LC FILTER

The designing LC filter, we must know the maximum voltage (v_m) in order to calculate the value of this filter, due to the voltage from that inverter is an unstable output voltage. So, it is necessary to add on a filter circuit in the system for preventing harmonic distortion enter the electrical system by using this parallel capacitance and series inductance as shown in Fig 9 and 10, thus reducing costs and losses compared with L filter [18]. The selection of the inductance (L) and capacitance (C) in a filter can be calculated from these equations.

$$V_m = V_{rms}\sqrt{2} \tag{15}$$

$$L < \frac{0.03V_m}{2\pi f I_{Lmax}} \tag{16}$$

$$f_c < \frac{1}{10} f_{sw} \tag{17}$$

$$C = \frac{1}{(2\pi f_c)^2 L} \tag{18}$$

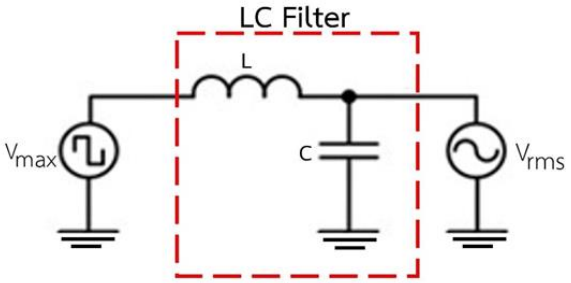

Fig. 9. LC filter circuit

Where I_{Lmax} is the maximum RMS value of the load current, the frequency of the output voltage is 'f'. So, f_{sw} is the switching frequency of inverters and f_c is the cutoff frequency. Moreover, these parameters of that filter can calculate from equations (15) -(18), which had shown in table III.

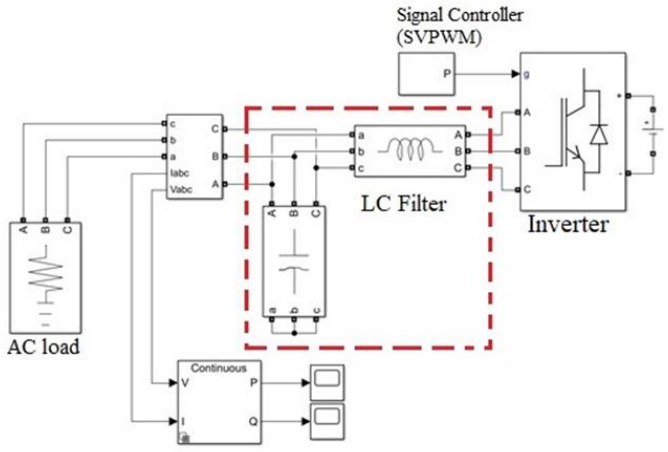

Fig. 10. Model of the DC to AC converter and LC filter with three-phase load

TABLE III. PARAMETERS OF A LC FILTER CIRCUIT

Maximum Voltage	V_{MAX}	537.4 V
Root mean square Voltage	V_{rms}	380 V
Frequency of the output voltage	f	50 Hz
L Filter	L	$2.2518e^{-4}$ H
Cut-off frequency	f_c	200 Hz
Switching frequency	f_{sw}	2000 Hz
C Filter	C	0.0113 F
Maximum RMS value of the load current	$I_{L,MAX}$	75.97 A

VII. SIMULATION RESULT

The proposed model of the hybrid system has been implemented in Matlab/Simulink program. In order to evaluate the energy transmission performance, the first simulation of that system is achieved by transmitting voltage through the boost converter from PV system, under varying the radiance of 600-1000 W/m2 at 5 s to the inverter system as shown in Fig. 11 and 12. The second scenario is the voltage sending values of a boost converter from fuel cell with a constant energy to point connection of the PV system for supporting voltage transfer to the AC load as shown in Fig. 13 and 14. Moreover, the duty cycle signals of both control systems are plotted in Fig. 15 and 16, for those graphs above mentioned the switching signal had different signal because of the PV system could produce voltage is 425V, but the based voltage of fuel cells is 625V, therefore, was used different duty cycle values. In the third section, the voltage of AC load had shown in Fig. 17, which that AC voltage (phase to phase) is less than the input voltage of an inverter system due to the inverter controller used the modulation index value only just 40% for transmitting the voltage as the load requires. Finally, the test of the hybrid system has been carried out. In this manner, Fig. 18 shows the output powers of that system or load power (P-load), which the testing was started by the AC load is 10 kW and then that increases the load demand from 10 kW to 20, 30, 40, and 50 kW, respectively. From the experimental result of the power transmission, it was found that the system design was able to transmit the electrical voltage at the requirements of 10kW, 20 kW and 30 kW. However, when the requirement was over 30 kW the system could not transmit the electric power as requested.It was necessary to increase the capacitor in LC filter circuit or adjust the modulation index value of an inverter system. In this research, there was the addition of capacitor in the LC filter circuit from 0.0113 to 0.0125F. This resulted in the ability to transmit the electric power as requested. According in Fig. 19, but the electric voltage in transmission would slightly increase as the electric power increased.

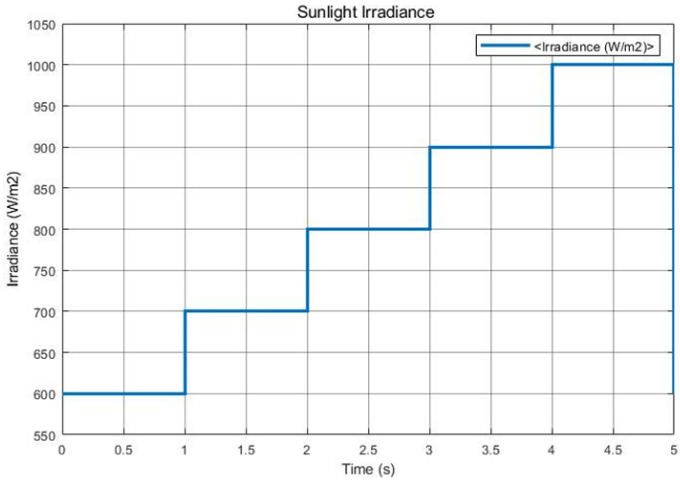

Fig. 11. Sunlight Irradiance

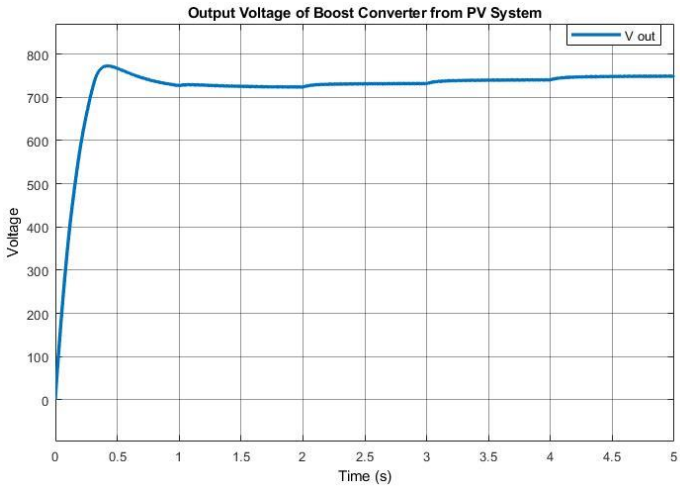

Fig. 12. Output voltage of boost converter from PV system

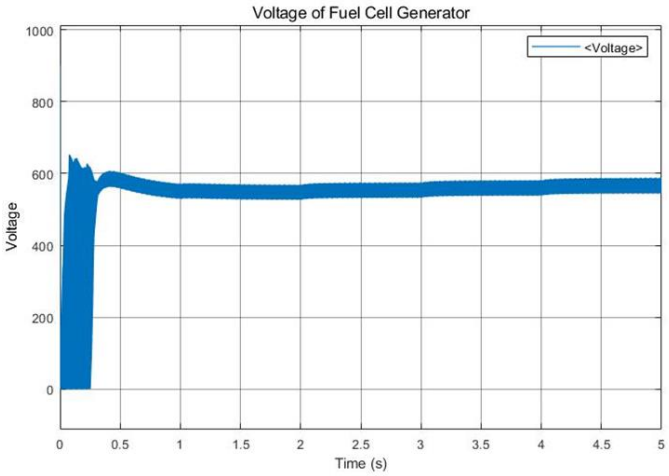

Fig. 13. Voltage of fuel cell generator

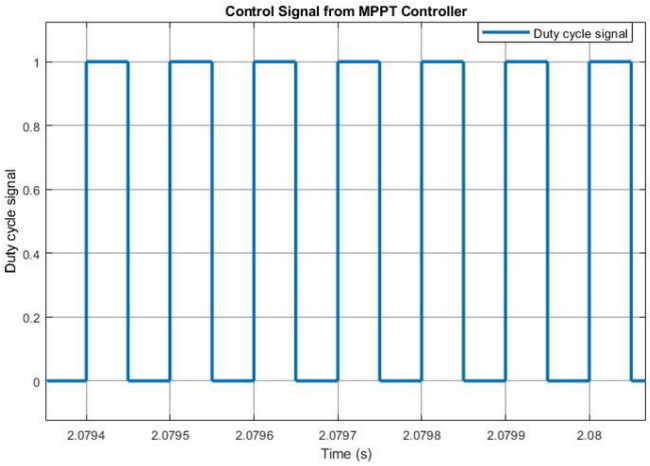

Fig. 16. Control signal from MPPT (P&O) within boost converter

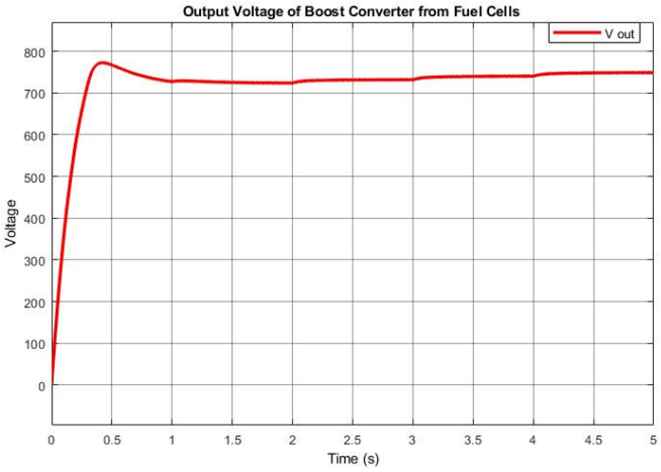

Fig. 14. Output voltage of boost converter from fuel cell generator

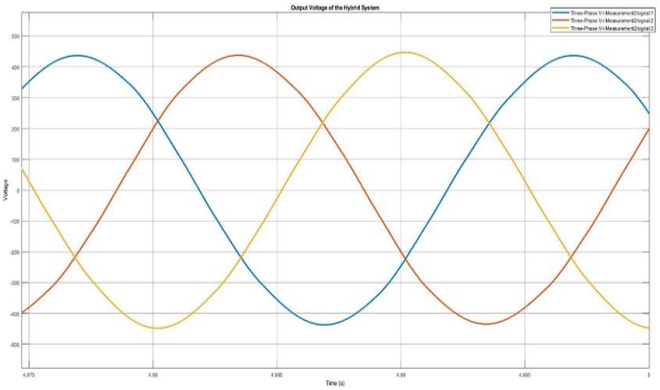

Fig. 17. Output voltage of the hybrid system for AC load

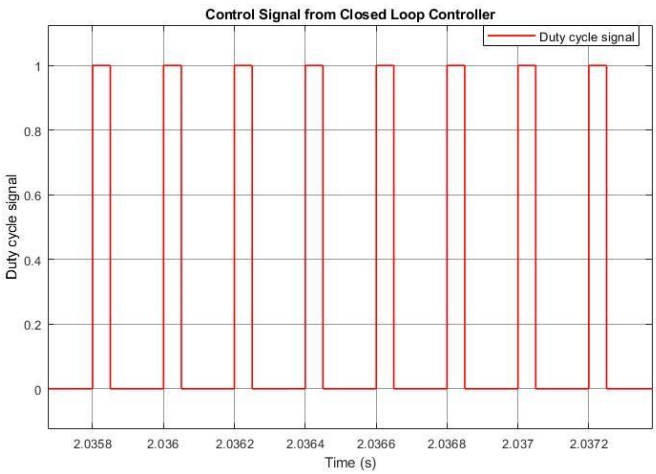

Fig. 15. Control signal from closed loop controller within boost converter

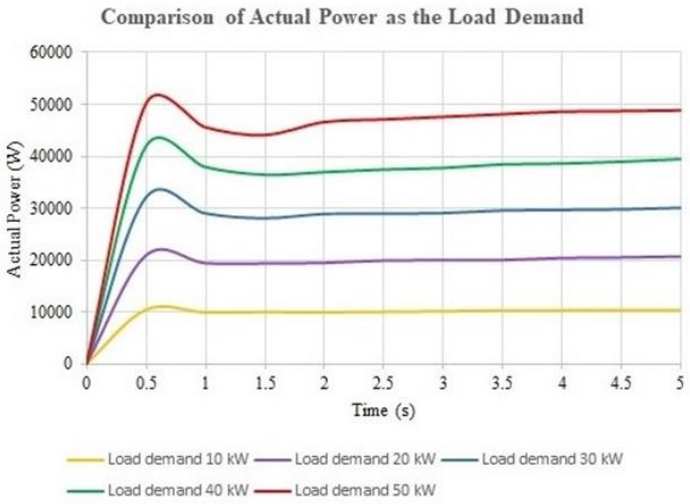

Fig. 18. Comparison of actual power as the load demand

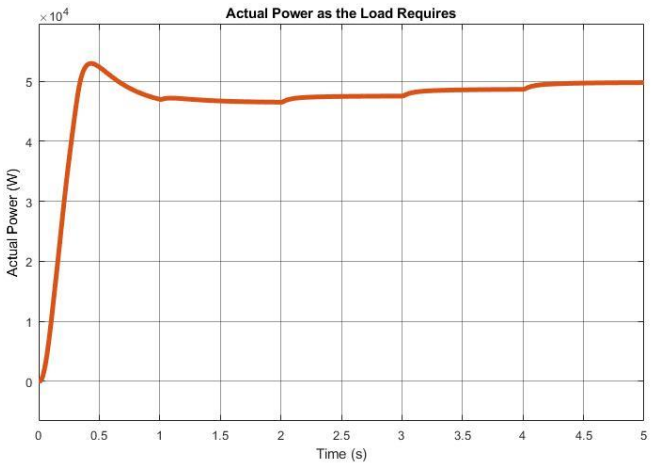

Fig. 19. Actual power as the load requires, After improved

VIII. CONCLUSIONS

In this research, a design of that hybrid system has been designed and performed. It has been understood that the proposed system design with connections of PV and fuel cell systems for transmitting energy to the load is working very well due to could transfer power at voltage frequency constant and improving the problem as load requirement. Moreover, also analyzed the working principle of this system, which started with using both PV and fuel cell systems to be the source energy and then send that energy on an AC load, but need to increase voltages from the boost converter, convert current with an inverter and adjust signal by the LC filter circuit for imparting to the load as shown the fully element of that system in Fig. 20. In the future can bring this paper for applying with electrical grid or expand this system at larger loads

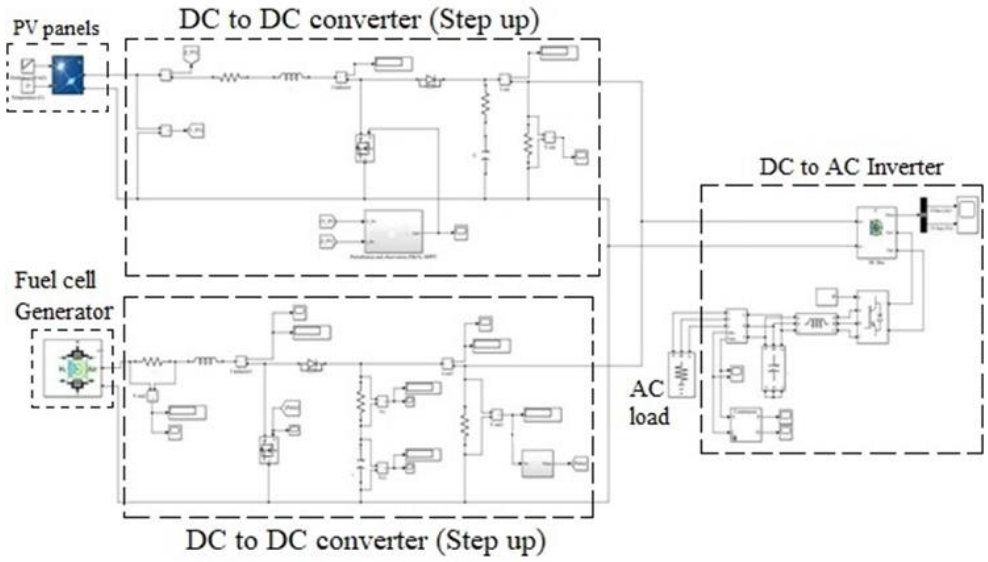

Fig. 20. Model of the element hybrid system circuit

REFERENCES

[1] Arjav Harjai, Abhishek Bhardwaj and Mrutyunjaya Sandhibigraha. " STUDY OF MAXIMUM POWER POINT TRACKING (MPPT) TECHNIQUES IN A SOLAR PHOTOLTAIC ARRAY " Department of Electrical Engineering National Institute of Technology Rourkela-769008, Orissa. pp.1-49

[2] Andrea, E. Manana, M. Ortiz, A. Renedo, C. Eguiluz, L.I. Perez and S. Delgado F. " A simplified electrical model of small PEM fuel cell " Vol. 1, 4 April 2006.

[3] Bhalchandra V" Chikate and Y"A" Sadawarte. " The Factors Affecting the Performance of Solar Cell " International Conference on Quality Up-gradation in Engineering, Science and Technology. pp.1-5.

[4] G. Sreenivasa Reddy, T. Bramhananda Reddy and M. Vijaya Kumar. " A MATLAB based PV Module Models analysis under Conditions of Nonuniform Irradiance " International Conference on Power Engineering, Computing and Control, 2-4 March 2017. pp. 974-983.

[5] K. Kalyan Kumar, R. Bhasker and Hemanth Koti. " Implementation of MPPT algorithm for solar photovoltaic cell by comparing short-circuit method and incremental conductance method. " Procedia Technology 12 (2014) pp. 705-715

[6] M. R. AlRashidi, K. M. El-Nagger and M. F. AlHajri. " Paramters Estimation of Double Diode Solar Cell Model " International Journal of Electrical and Computer Enginerring, Vol. 7, 2013, pp. 118-121.

[7] M. A. Ebrahim, Adham Osama, Khaled Mohamed Kotb and Fahmy Bendary. " Whale inspired algorithm based MPPT controllers for grid-connected solar photovoltaic system " Special Issue on Emerging and Renewable Energy: Generation and Automation, 162 (2019), pp. 77-86.

[8] Razman Ayop and Chee Wei Tan, " Design of boost converter based on maximum power point resistance for photovoltaic applications " Solar Energy 160 (2018), pp. 322-335.

[9] Ratna Ika Putri, Sapto Wibowo and Muhamad Rifai. " Maximum power point tracking for photovoltaic using incremental conductance method " International Conference on Sustainable Energy Engineering and Application, ICSEEA 2014, 68 (2015), pp. 22-30.

[10] S. Sheik Mohammed and D. Devaraj. " Simulation and Analysis of Stand-alone Photovoltaic System with Boost Converter using MATLAB/Simulink " International Conference on Circuit, Power and Computing Technologies, 2014. pp. 814-821.

[11] Srinivasan. V, J. Hameed Hussain. " EXPERIMENTAL ANALSIS OF PARALLEL AND SERIES CONNECTED SOLAR PV SYSTEM UNDER EFFECT OF SHADOW CONDITIONS " International Journal of Pure and Applied Mathematics, Vol. 116, 14 (2017), pp. 421-426.

[12] Vivek Tamrakar, S.C. Gupta and Yashwant Sawle. " SINGLE-DIODE AND TWO-DIODE PV CELL MODELING USING MATLAB FOR STUDYING CHARACTERISTICS OF SOLAR CELL UNDER VARYING CONDITIONS " Electrical & Computer Engineering: An International Journal, Vol. 4 , June 2015, pp. 67-77.

[13] Bouthaina Madaci, Erol Hurt, Rachid Chenni and Kamei Eddjne Hemsas. " Design and control of a stand-alone hybrid power system " International Journal of Hydrogen energy (2016), pp. 1-12.

[14] Youssef Cheddadi, Fatime Errahimi and Es-sbai Najia. " Design and verification of photovoltaic MPPT algorithm as an automotive based embedded software " Sotar Energy 171 (2018), pp. 414-425.

[15] Doudou N. Luta and Atanda K. Raji. " Comparing Fuzzy rule-based MPPT techniques for fuel cell stack pplications " International Conference on Power and Energy System Engineering, CPESE 2018, 19-21 Sptember 2018, Nagoya, Japan. pp. 177-182.

[16] Myada Shadoul, Rashid Al Abri, Hassan Yousef and Mahmoud Massoud. " DC-DC Boost Converter Controller Design for PV Applications " IEEE-GCC Conference and Exhibition, 9th (2017).

[17] K. Vinoth Kumar, Prawin Angel Michael, Joseph P. John and S. Suresh Kumar. " SIMULATION AND COMPARISON OF SPWM AND SVPWM CONTROL FOR THREE PHASE INVERTER" Vol. 5, ARPN JOURNAL of Engineering and Applied Sciences. 7 July 2010. pp. 61-74.

[18] Mojgan Hojabri and Mehrdad Hojabri. " DESIGN, APPLICATION AND COMPARISON OF PASSIVE FILTER FOR THREE-PHASE GRID-CONNECTED RENEWABLE ENERGY SYSTEMS " ARPN Journal of Engineering and Applied Sciences, Vol. 10, 22 December 2015.

[19] Emad Talib Hashim and Shahad Qasim Khazaal. " Modelling and Outout Power Evaluation of Series Parallel Photovoltaic Modules " International Journal of Computer Applications, Vol. 158, 8 January 2017, pp. 35-46.

[20] Gokhan Altintas, Mehmet Onur Gulbahce and Derya Ahmet Kocabas. " Nonideal Analysis, Design and Voltage Mode Control of a Boost Converter " International Scientific Conference on Power and Electrical Engineering of Riga Technical University, 57th 2016

[21] Huang Min, Blaabjerg Frede, Yang Yongheng and Wu Weimin. " Step by step Design of a High Order Power Filter for Three-Phase Three-Wire Grid-connected Inverter in Renewable Energy System " IEEE International Symposium on power Electronics for Distributed Generation Systems, 4th 2013.

[22] Jitendra Nath Ral. " Design and Analysis of Dc-Dc Boost Converter " September 2016.

[23] Krismadinata, Nasrudin Abd. Rahim Hew Wooi Ping and Jeyraj Selvaraj. " Photovoltaic module modeling using Simulink/matlab " International Conference on Sustainable Future for Human Security SUSTAIN 2012, 17 (2013), pp. 537-546.

[24] Laxmi Kant Dwivedi, Vikram singh, Arjun Pareek and Prabhat Yadav. " MATLAB/SIMULINK based study of series-parallel connected photovoltaic system under partial shaded condition " International Research Journal of Engineering and Technology, Vol. 3, October.

[25] Myada Shadoul, Rashid Al Abri, Hassan Yousef and Mahmoud Massoud. " DC-DC Boost Converter Controller Design for PV Applications " IEEE-GCC Conference and Exhibition, 9th (2017).

Conjugate Versus Identical Matching in Waveguide Medium with Complex Characteristic Impedance

Apisak Worapishet
Mahanakorn Microelectronics Research Center, MMRC
Mahanakorn University of Technology
140 Cheumsampan Rd., Nong-Chok, Bangkok, Thailand.
Email: apisak@mut.ac.th

***Abstract*—This paper provides an analytical treatment to address the unconventional design scenario facing by RF engineers on state-of-the-art wireless communication circuits and systems of which electromagnetic wave media are becoming increasingly lossy yielding a complex characteristic impedance. Based upon the power analysis using a phasor representation, the complex characteristic impedance is attributed to an imbalance of electric and magnetic fields in a wave medium caused by the medium loss that results in the voltage/current amplitude ratio different from the value supported by the medium for propagation, thereby creating stored reactive power on the medium. A detailed analysis on the conjugate and identical matchings under a complex characteristic impedance reveals an insightful physical mechanism that underlies the complex power flow on the TL towards the load termination under both conditions. It can be deduced that the identical matching is a preferred choice when an adverse impact from the load reflection is not fully recognised. Although the maximum power transfer cannot be achieved, such a design is more robust to self-interference which may entirely disrupt the communications.**

Keywords—Conjugate matching; maximum power transfer; transmission line; characteristic impedance; (key words)

I. INTRODUCTION

In radio-frequency (RF) circuits and systems typically equipped with waveguide structures, two main matching conditions, namely the conjugate matching (CM) and the identical matching (IM), are common practice for designing the load termination. In principle, whereas the CM enables *maximum* transfer of power from the wave travelling on the waveguide to the load, the IM results in less power transfer but there is no wave reflection.

Consider a transmission line (TL) schematically represented as a two-wire structure to support guided wave propagation in Fig. 1, with a characteristic impedance $\mathbf{Z}_O$ and a load impedance $\mathbf{Z}_L$. Whereas the load termination under the conjugate matching condition is $\mathbf{Z}_L = \overline{\mathbf{Z}_O}$ (the upper bar denotes the complex conjugate operator), the termination under the identical matching is $\mathbf{Z}_L = \mathbf{Z}_O$, assuming the source impedance is identically matched to $\mathbf{Z}_O$.

It is typical in practice to assume that the characteristic impedance $\mathbf{Z}_O$ possesses only a real value. This yields in an equivalent load condition for IM and CM, i.e., $\mathbf{Z}_L = \mathbf{Z}_O = \overline{\mathbf{Z}_O}$. However, when $\mathbf{Z}_O$ becomes a complex value, particularly when the waveguide medium is lossy [1], the IM and CM conditions are different. As a consequence, the question arises, "How do we choose the load condition for the design task at hand?".

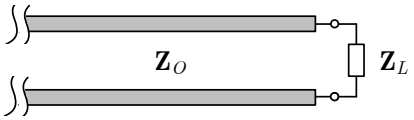

Fig. 1. TL schematic of characteristic impedance $\mathbf{Z}_O$ and load $\mathbf{Z}_L$.

This paper seeks to answer this unconventional design scenario that starts to manifest itself in state-of-the-art RF circuits and systems where the medium losses becomes more common. This is typified by the emerging 5G mobile systems with the operating frequency bands being pushed towards the millimeter wave region and beyond [2]. Another emerging application involving a complex characteristic impedance is the body-channel wireless communication [3].

We start by outlining the basic theoretical foundation for subsequent analysis in Section II. Also, the description on the complex characteristic impedance, and the general analytical investigation of the IM and CM conditions are given. More specific and insightful discussion on the operating mechanism that differentiates between the IM and CM at the load termination is then provided in Section III. Finally, conclusion is given in Section IV.

II. BASIC THEORY

In this section, we briefly summarize the basic concepts that will be employed in the subsequent analysis, with particular emphasis on complex power flow in an electrical network. To make it more accessible to general readers, the variables associated with the waves travelling along a waveguide in the derivation are voltage (V) and current (I) signals, instead of electric (**E**) and magnetic (**H**) fields. Note that V is related to **E**, and I is related to **H**, depending on the waveguide structure.

A. Time-Domain Signal and Its Phasor Form

A time-domain sinusoidal signal, $x(t)$, can be written as a sum of two complex exponentials.

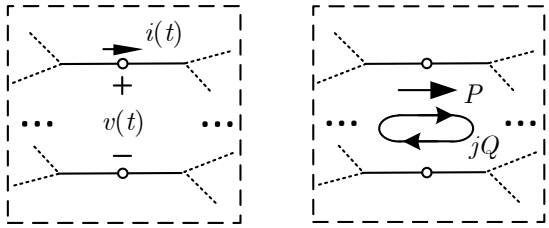

Fig. 2. Terminal voltage and current within a network for power calculation.

$$x(t) = |X| \cos(\omega t + \theta_X) = \frac{\mathbf{X}}{2} e^{+j\omega t} + \frac{\overline{\mathbf{X}}}{2} e^{-j\omega t} \quad (1)$$

where $\mathbf{X} = |X| e^{j\theta_X} =$ is the phasor representation of $x(t)$. The relation between $x(t)$ and its phasor form $\mathbf{X}$ is via the projection onto the real axis, as given by

$$x(t) = \mathrm{Re}\left(\mathbf{X} e^{+j\omega t}\right) \quad (2)$$

where Re(·) is the real part operator. Due to its simplicity, the phasor form is normally employed to analyse and visualise the voltages, currents, powers and their relationship in electrical networks.

B. Complex Power

Consider power flow between a pair of terminals within a network as shown in Fig. 2(a) with sinusoidal voltage $v(t)$ and current $i(t)$ given by

$$v(t) = |V| \cos(\omega t + \theta_V) \quad (3a)$$

$$i(t) = |I| \cos(\omega t + \theta_I) \quad (3b)$$

The instantaneous power $p(t)$ exchanged between the terminals is the product $v(t) \cdot i(t)$. By using (3a) and (3b), along with the trigonometry identities, $\cos(u) \cdot \cos(v) = \cos(u - v) + \cos(u + v)$ and $\cos(u + v) = \cos(u) \cdot \cos(v) - \sin(u) \cdot \sin(v)$, the instantaneous power can be written as

$$p(t) = P \cdot [1 + \cos(2\omega t)] + Q \cdot [\sin(2\omega t)] \quad (4a)$$

with

$$P = \frac{|VI|}{2} \cos(\theta_V - \theta_I) \quad (4b)$$

$$Q = \frac{|VI|}{2} \sin(\theta_V - \theta_I). \quad (4c)$$

The terms P and Q can also be determined by using the phasor representations $\mathbf{V} = |V| e^{j\theta_V}$ for $v(t)$ and $\mathbf{I} = |I| e^{j\theta_I}$ for $i(t)$, as given by

$$\mathbf{S} = P + jQ = \mathbf{V} \cdot \bar{\mathbf{I}} = \frac{|VI|}{2} e^{j(\theta_V - \theta_I)}. \quad (5)$$

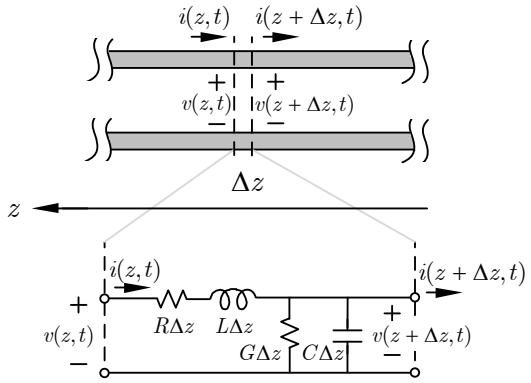

Fig. 3. Equivalent TL model based on lumped element.

The equation $\mathbf{S} = P + jQ$ is called the complex power with P being the *real* power, Q being the *reactive* power, and the magnitude $|\mathbf{S}| = \sqrt{P^2 + Q^2}$ being the *apparent* power.

Based on (4) and (5), the real power P represents the time-average power dissipation and its pulsations. On the other hand, the reactive power Q represents the power exchange with *zero* time-average or lossless/stored power. A diagram illustrating the P and Q components of the complex power flow is given in Fig. 2(b).

It is important to point out that the real/reactive values of the complex power are dependent on the phase difference, $\theta_V - \theta_I$, between the sinusoidal voltage and current signals. In particular, the complex power has only real power when $\theta_V - \theta_I = 0$, and only reactive power when $\theta_V - \theta_I = \pm\pi / 2$ or right angle.

C. Voltage and Current Waves on TL

A small section of the TL schematically represented as a two-wire conductor terminated by the load $\mathbf{Z}_L$ of Fig, 1(a) can be modelled by an equivalent distribution of lumped R, L, G, C network as shown in Fig. 3, where R is the series resistance per unit length (Ohm/m), L is the series inductance per unit length (H/m), G is the shunt conductance per unit length (S/m), and C is the shunt capacitance per unit length (F/m). Note that L and C are lumped equivalent circuit models related to the magnetic field **H** and electric field **E** along the line, respectively. Also, R and G are lumped circuit models related to the losses associated with the **H** and **E** fields, respectively.

The total voltage and current waves along the TL consists of waves travelling in the positive and negative z directions, which can be given in the time-domain by [1]

$$v(z,t) = |V^+(0)|\cos(\omega t - \beta z + \theta_V^+)e^{-\alpha z} + |V^-(0)|\cos(\omega t + \beta z + \theta_V^-)e^{+\alpha z} \quad (6a)$$

$$i(z,t) = |I^+(0)|\cos(\omega t - \beta z + \theta_I^+)e^{-\alpha z} - |I^-(0)|\cos(\omega t + \beta z + \theta_I^-)e^{+\alpha z} \quad (6b)$$

In view of the phasor representation, the total waves are equivalently given by

$$\mathbf{V}(z) = \mathbf{V}^+(0)e^{-\gamma z} + \mathbf{V}^-(0)e^{+\gamma z} = \mathbf{V}^+(0)\left[e^{-\gamma z} + \Gamma e^{+\gamma z}\right] \quad (7a)$$

$$\mathbf{I}(z) = \mathbf{I}^+(0)e^{-\gamma z} - \mathbf{I}^-(0)e^{+\gamma z} = \frac{\mathbf{V}^+(0)}{\mathbf{Z}_O}\left[e^{-\gamma z} - \Gamma e^{+\gamma z}\right] \quad (7b)$$

where $\mathbf{V}^{+/-}(0)$ and $\mathbf{I}^{+/-}(0)$, respectively, denote the phasors of the travelling voltage and current waves at the load point where $z = 0$. The $e^{-\gamma z}$ term denotes the *forward* or *incident* wave propagating in the $+z$ direction, and the $e^{+\gamma z}$ term denotes the *backward* or *reflected* wave propagating in the -z direction. The complex propagation constant γ is given by

$$\gamma = \alpha + j\beta = \sqrt{(R + j\omega L)(G + j\omega C)} \quad (8)$$

where α is the attenuation constant in Nepers/m, and β is the phase constant in rad/m. In (7), the voltage and current waves are related via the characteristic impedance $\mathbf{Z}_O$ of the TL, with

$$\frac{\mathbf{V}^+(z)}{\mathbf{I}^+(z)} = \frac{\mathbf{V}^-(z)}{\mathbf{I}^-(z)} = \mathbf{Z}_O = \sqrt{\frac{R + j\omega L}{G + j\omega C}} \quad (9)$$

Also, the incident waves $\mathbf{V}^+$, $\mathbf{I}^+$ are related to their corresponding reflected waves $\mathbf{V}^-$, $\mathbf{I}^-$ via the reflection coefficient Γ at the load, where

$$\Gamma = \frac{\mathbf{V}^-(0)}{\mathbf{V}^+(0)} = \frac{\mathbf{I}^-(0)}{\mathbf{I}^+(0)} = \frac{\mathbf{Z}_L - \mathbf{Z}_O}{\mathbf{Z}_L + \mathbf{Z}_O} \quad (10)$$

Fig. 4(a) illustrates the forward/incident and backward/ reflected components of the phasors $\mathbf{V}(z)$ and $\mathbf{I}(z)$ at a distance l (or $z = -l$) from the load.

D. Complex Characteristic Impedance

One major mechanism that leads to a complex $\mathbf{Z}_O$ is the loss associated with the propagating medium [1], This includes the loss in the medium's permittivity that attenuates the voltage waves (related to electric field), and the loss in the permeability that attenuates the current waves (related to magnetic field). When the attenuated voltage and current results in the voltage/current amplitude ratio different from the value supported by the medium for wave propagation, a fraction of the voltage or current is not able to propagate further, hence becomes stationary. The stationary field only exchanges its energy locally with its surrounding space and is thus also called a stored field. Since the stored reactive field results in a non-zero phase difference, $\theta_V - \theta_I$, between the sinusoidal voltage and current signals, giving rise to a complex characteristic impedance $\mathbf{Z}_O$.

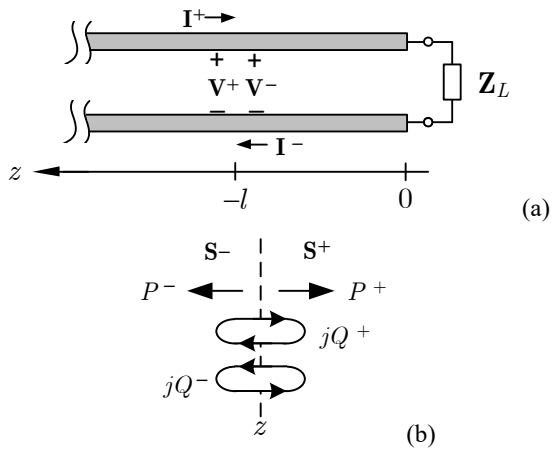

Fig. 4. Phasor representation of (a) voltage and curretn waves, (b) complex power flow on TL.

Typical in a general medium, the permittivity loss is significantly higher. Thus, the stored reactive field is of current or magnetic type, and $\mathbf{Z}_O$ possesses a positive imaginary part. On the contrary, when the permeability loss is higher, $\mathbf{Z}_O$ possesses a negative imaginary part. For the case that the permittivity and permeability losses attenuates the voltage and current amplitudes in such a way that the voltage/current ratio supported by the media is still maintained, there is no stored field, and $\mathbf{Z}_O$ is a real-value. Based on (9), such a loss condition that yields a real $\mathbf{Z}_O$ is

$$R / L = G / C \quad (11)$$

where R and G are non-zero.

E. Complex Power Flow on TL

Based on the complex power equation in (5) and the total voltage/current wave equations in (7), the complex power flow on the TL with the load reflection coefficient Γ can be derived as

$$\begin{aligned}\mathbf{S} &= (\mathbf{V}^+(0)e^{-\gamma z} + \mathbf{V}^-(0)e^{+\gamma z})\cdot\overline{(\mathbf{I}^+(0)e^{-\gamma z} - \mathbf{I}^-(0)e^{+\gamma z})} \\ &= (\mathbf{V}^+(0)e^{-\gamma z} + \Gamma\cdot\mathbf{V}^-(0)e^{+\gamma z}) \\ &\quad \cdot\left(\frac{\overline{\mathbf{V}^+(0)}}{\overline{\mathbf{Z}_O}}e^{-\alpha z+j\beta z} - \overline{\Gamma}\cdot\frac{\overline{\mathbf{V}^+(0)}}{\overline{\mathbf{Z}_O}}e^{+\alpha z-j\beta z}\right) \\ &= \frac{|\mathbf{V}^+(0)|^2}{\overline{\mathbf{Z}_O}}\left(\underbrace{(\overbrace{e^{-2\alpha z}}^{\mathbf{S}^{++}} + \overbrace{\Gamma e^{+j2\beta z}}^{\mathbf{S}^{-+}})}_{\mathbf{S}^+=P^+ + jQ^+} - \underbrace{(\overbrace{|\Gamma|^2 e^{+2\alpha z}}^{\mathbf{S}^{--}} + \overbrace{\overline{\Gamma}e^{-j2\beta z}}^{\mathbf{S}^{+-}})}_{\mathbf{S}^-=P^- + jQ^-}\right)\end{aligned} \tag{12}$$

To obtain the operational insight, the complex power in (12) is separated into two main components $\mathbf{S}^+$ and $\mathbf{S}^-$, which represent the power flow in the positive and negative z directions as determined by the incident and reflected current waves $\mathbf{I}^+$ and $\mathbf{I}^-$, respectively. In addition, both $\mathbf{S}^+$ and $\mathbf{S}^-$ contain the cross-product terms between the incident and reflected voltage/current waves explicitly shown as $\mathbf{S}^{-+}(=\mathbf{V}^-\overline{\mathbf{I}^+})$ and $\mathbf{S}^{+-}(=\mathbf{V}^+\overline{\mathbf{I}^-})$ in (12). This indicates that while the voltage/current waves along the TL can be *completely decomposed* into the incident/reflected components, the power flow resulting from the waves must take into account their interaction. A calculation of power resulting from individual incident and reflected waves which include only $\mathbf{S}^{++}$ and $\mathbf{S}^{--}$ is not physically meaningful. One important implication from the interaction is that the cross-product terms $\mathbf{S}^{-+}$ of $\mathbf{S}^+$ and $\mathbf{S}^{+-}$ of $\mathbf{S}^-$ can indeed impact the complex power flow in the forward and backward directions. Also in the equation, as the wave propagates, its associated power decays exponentially according to the attenuation factor, $e^{\pm 2\alpha z}$, due to electric and magnetic dissipation in the lossy medium that forms the TL.

As illustrated in Fig. 4(b), the real part $P^{+/-}$ of the complex power $\mathbf{S}^{+/-}$ is attributed to the flow of power associated with the waves propagating in the forward/backward direction. On the other hand, the imaginary part $Q^{+/-}$ of the complex power $\mathbf{S}^{+/-}$ is attributed to the localised stored power of the fields at a point z on the TL. The complex power equation in (12) is central to the subsequent analysis.

III. Complex Power Flow Under IM and CM

A. Real Characteristic Impedance $\mathbf{Z}_O = R_O$

In most practical scenarios where a wave medium is lossless, the characteristic impedance $\mathbf{Z}_O$ is a real value. For a lossy medium, a real value $\mathbf{Z}_O$ is possible under the condition given in (11).

A.1 IM and CM Conditions

For a TL with $\mathbf{Z}_O = R_O$, the IM and CM at the load termination are identical since $\mathbf{Z}_L = \mathbf{Z}_O = \overline{\mathbf{Z}_O} = R_O$. This yields $\Gamma = (\mathbf{Z}_L - R_O)/(\mathbf{Z}_L + R_O) = 0$ and there are no reflected wave components. By using (12), the complex power flow $\mathbf{S}$ along the TL is given by

$$\mathbf{S} = \underbrace{P_{ma}e^{-2\alpha z}}_{\mathbf{S}^{++}=P} + j\underbrace{0}_{Q} \tag{13}$$

where $P_{ma} = |\mathbf{V}^+(0)|^2/R_O$ is the *maximum* real power from the incident wave propagating in the forward direction towards the load at $z = 0$. The equation indicates that there is only a real power flow of the component $\mathbf{S}^{++}$ due to the incident voltage/current waves along the TL.

A.2 Mismatch Condition

It is instructive to investigate the complex power flow under a load mismatch, $\mathbf{Z}_L \neq R_O$, which gives rise to reflected wave components travelling in the backward direction. These reflected waves interact with the incident counterparts, modifying the flow of power along the TL as explained in Section II. By using (12), the complex power flow under this condition normalized to the maximum available power P_{ma} is given by

$$\begin{aligned}\mathbf{S}_n = \frac{\mathbf{S}}{P_{ma}} &= (\overbrace{e^{-2\alpha z}}^{\mathbf{S}_n^{++}} - \overbrace{|\Gamma|^2 e^{+2\alpha z}}^{\mathbf{S}_n^{--}}) + \overbrace{\Gamma e^{+j2\beta z}}^{\mathbf{S}_n^{-+}} - \overbrace{\overline{\Gamma}e^{+j2\beta z}}^{\mathbf{S}_n^{+-}} \\ &= \underbrace{(\overbrace{e^{-2\alpha z} - |\Gamma|^2 e^{+2\alpha z}}^{\mathbf{S}_n^{++}-\mathbf{S}_n^{--}})}_{P_n} + j\underbrace{\overbrace{2\,\mathrm{Im}\left(\Gamma e^{+j2\beta z}\right)}^{\mathbf{S}_n^{-+}-\mathbf{S}_n^{+-}}}_{Q_n}\end{aligned} \tag{14}$$

The normalisation is applied for notational convenience and ease of discussion. In the equation, $\mathbf{S}_n$ is divided into their constituent components as indicated in (12). Under a real $\mathbf{Z}_O$ and mismatch conditions, the components $\mathbf{S}^{++}$ and $\mathbf{S}^{--}$ are real valued, indicating power flow of the incident and reflected waves, respectively. Although the cross-product terms $\mathbf{S}^{-+}$ and $\mathbf{S}^{+-}$ possess flow of real power, they are in opposite directions and hence cancelled out, leaving only localised stored reactive power along the TL, known as the standing waves.

Under a lossless TL ($\alpha = 0$) and $\mathbf{Z}_L = 2R_O$, Fig. 5(a) shows the numerical plot of the normalized complex power $\mathbf{S}_n$ versus z using (14). It is noticed that while the normalized real power flow P_n is constant, the normalized reactive power Q_n of the standing waves varies along the TL. Also, since

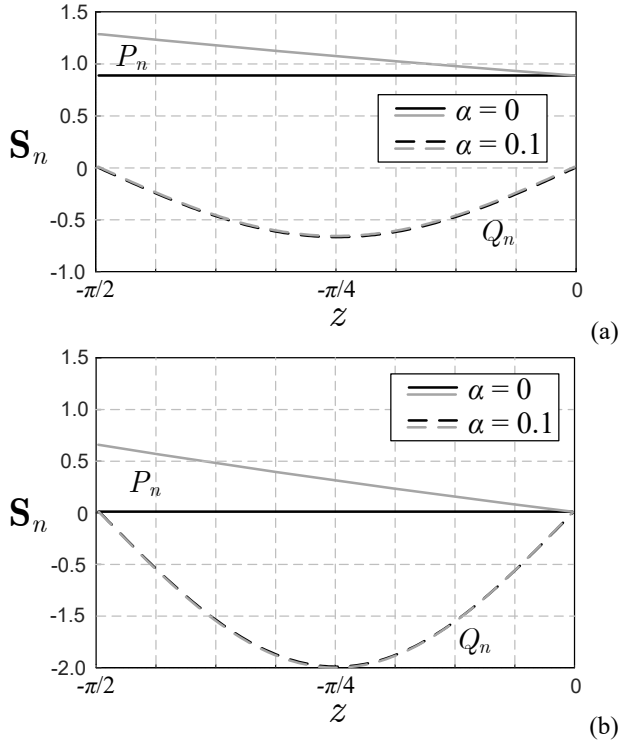

Fig. 5. Complex power flow on TL under at $\alpha = 0$ and 0.1 with (a) $\mathbf{Z}_O = R_O$, (b) $\mathbf{Z}_O = 0$ and ∞.

$P_n(0)$ is less than unity, and the real power delivered to the load is less than P_{ma} under the CM condition. Under a lossy TL with $\alpha = 0.1$, Fig. 5(b) shows $\mathbf{S}_n$ versus z. In this case, P_n decays along the TL due to the loss, while Q_n is maintained as in the lossless case.

Let us consider the extreme mismatch where the load is either short ($\mathbf{Z}_L = 0$) or open ($\mathbf{Z}_L = \infty$), which yield $\Gamma = -1$ and $+1$, respectively. By using (14), we have

$$\mathbf{S}_n = \underbrace{e^{-2\alpha z}(1 - e^{+4\alpha z})}_{P_n} \mp j \underbrace{2\sin(2\beta z)}_{Q_n} \tag{15}$$

Under the lossless case at $\alpha = 0$, we have $P_n = 0$ and $Q_n \neq 0$ as shown in the numerical plot of Fig. 5(b). Thus, there is no net propagation of wave, only the stored reactive power or standing waves along the TL. Through the investigation of the phase difference, the total voltage and current waves are perfectly at right angle to each other at any point along the TL, thereby causing the complex power flow to have only the reactive power Q_n. Note that this makes the TL with short or open termination an energy storage element widely employed in most RF circuits. Under a lossy case where $\alpha > 0$, we have $P_n > 0$ and $Q_n \neq 0$ as also shown in Fig. 5(b), and thus there is non-zero net loss from the waves attenuation, reducing the quality factor of the TL-based energy storage element.

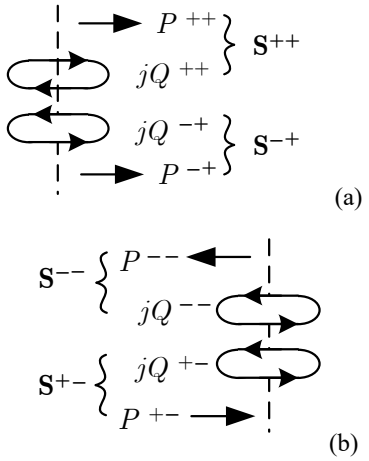

Fig. 6. Complex power flow under $\mathbf{Z}_L = R_O$ and CM for (a) forward components $\mathbf{S}^+$, (b) backward components $\mathbf{S}^-$.

B. Complex Characteristic Impedance $\mathbf{Z}_O = R_O + jX_O$

As described in Section II, a complex characteristic impedance is attributed to a lossy wave medium that attenuates the **E** and/or **H** fields associated with the voltage and current waves, in such a way that causes the fields ratio to deviate from the value supported by the medium for propagation. As a result, a fraction of the less attenuated field becomes stationary yielding locally stored power along the TL, causing the characteristic impedance to be a complex value.

B.1 IM Condition

For a TL with $\mathbf{Z}_O = R_O + jX_O$, the IM condition at the load $\mathbf{Z}_L = \mathbf{Z}_O$ yields $\Gamma = 0$ and there are no reflected wave components. By using (12) and rearranging the equation in terms of the maximum available power $P_{ma} = |\mathbf{V}^+(0)|^2 / R_O$, it can be shown that the normalized power flow is given by

$$\mathbf{S}_n = \frac{\mathbf{S}}{P_{ma}} = \overbrace{\frac{1}{1 + \frac{X_O^2}{R_O^2}}\left(1 + j\frac{X_O}{R_O}\right)e^{-2\alpha z}}^{\mathbf{S}_n^{++}} = \overbrace{\underbrace{\frac{e^{-2\alpha z}}{1+\sigma^2}}_{P_n} + j\underbrace{\frac{\sigma e^{-2\alpha z}}{1+\sigma^2}}_{Q_n}}^{\mathbf{S}_n^{++}} \tag{16}$$

where $\sigma = X_O / R_O$. It is evident from (16) that the complex power is only due to the incident wave component $\mathbf{S}^{++}$, and composed of both real and reactive power. The presence of the

reactive power is attributed to the stored **E** or **H** field left-behind as the incident waves propagates. As a consequence, even with no reflection under a complex $\mathbf{Z}_O$, there exists standing waves on the TL. Moreover, the real power delivered to the load $\mathbf{Z}_L = \mathbf{Z}_O$ can be given by

$$P = \mathrm{Re}\left[\mathbf{S}(0)\right] = \underbrace{\frac{1}{1+\sigma^2}}_{P} P_{ma} < P_{ma} \qquad (17)$$

This is less than the maximum value available from the incident wave.

B.2 CM Condition

Under the CM with $\mathbf{Z}_L = \overline{\mathbf{Z}_O} = R_O - jX_O$, we have $\Gamma = -jX_O / R_O = -j\sigma$, and the normalized power flow obtained from (12) can be given by

$$\mathbf{S}_n = \overbrace{\frac{1+j\sigma}{1+\sigma^2}e^{-2\alpha z}}^{\mathbf{S}_n^{++}} - \overbrace{j\sigma\frac{1+j\sigma}{1+\sigma^2}e^{j2\beta z}}^{\mathbf{S}_n^{-+}} - \overbrace{\sigma^2\frac{1+j\sigma}{1+\sigma^2}e^{+2\alpha z}}^{\mathbf{S}_n^{--}} - \overbrace{j\sigma\frac{1+j\sigma}{1+\sigma^2}e^{-j2\beta z}}^{\mathbf{S}_n^{+-}} \qquad (18)$$

By setting $z = 0$ to investigate the power delivered to the load, the equation becomes

$$\mathbf{S}_n = \overbrace{\left(\frac{1}{1+\sigma^2}+\frac{j\sigma}{1+\sigma^2}\right)}^{\mathbf{S}_n^{++}} + \overbrace{\left(\frac{\sigma^2}{1+\sigma^2}-\frac{j\sigma}{1+\sigma^2}\right)}^{\mathbf{S}_n^{-+}} + \overbrace{\left(\frac{-\sigma^2}{1+\sigma^2}+\frac{-j\sigma^3}{1+\sigma^2}\right)}^{\mathbf{S}_n^{--}} + \overbrace{\left(\frac{\sigma^2}{1+\sigma^2}-\frac{j\sigma}{1+\sigma^2}\right)}^{\mathbf{S}_n^{+-}}$$
$$= \underbrace{1}_{\mathbf{S}_n^{++}+\mathbf{S}_n^{-+}} - \underbrace{j\sigma}_{\mathbf{S}_n^{--}+\mathbf{S}_n^{+-}} \qquad (19)$$

Similar to the previous cases, $\mathbf{S}_n$ is divided into its constituent components as indicated in (19) and illustrated in Fig. 6(a). For the forward power flow $\mathbf{S}_n^+$, the cross-product term $\mathbf{S}_n^{-+}$ due to the interaction between the reflected voltage $\mathbf{V}^-$ and incident current wave $\mathbf{I}^+$ not only cancels out the reactive power associated with the incident component $\mathbf{S}^{++}$, but also contributes additional real power to restore the maximum power P_{ma} available from the incident wave to the load. For the reflected power flow $\mathbf{S}_n^-$ as illustrated in Fig. 6(b), there is a cancellation of the real power components, leaving only the reactive power, which can be shown to equal

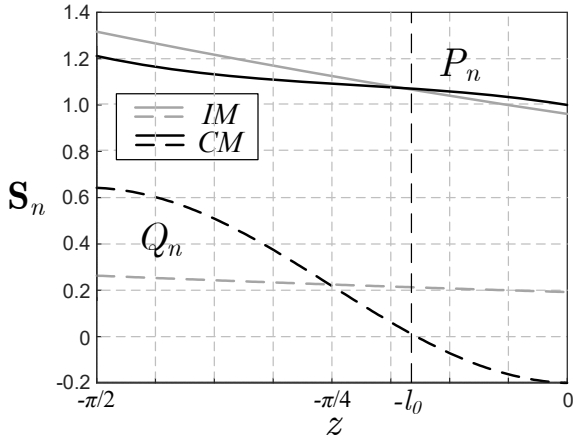

Fig. 7. Complex power flow on TL with complex $\mathbf{Z}_O$ under IM and CM conditions.

to the power in the reactive part $-jX_O$ of the load after denormalisation.

It is also instructive to investigate the complex power flow on the TL using (18). By setting $\alpha = 0.1$ and $\sigma = 0.05$, the numerical plots of $\mathbf{S}_n$, are given in Fig. 7. From $z = -l_0$ up to the load point at $z = 0$, the real power flow P_n is increased and the reactive power Q_n is decreased, as compared to their corresponding values under the IM condition also included in the figure. This is attributed to the incident/reflected waves interaction which creates backward reactive power opposite to that created along the TL with a complex $\mathbf{Z}_O$. At $z < -l_0$ however, the backward reactive power is reversed, thereby strengthening the net reactive power, hence resulting in less real power flow than the value under the IM condition.

IV. Summary

Complex wave power flow along a waveguide medium consists of real power attributed to travelling waves, and stored reactive power attributed to stationary or standing waves. A complex characteristic impedance $\mathbf{Z}_O$ is attributed to imbalance of losses in an electromagnetic wave medium which causes attenuation in the voltage and/or current waves in a way that makes their amplitude ratio different from the value supported by the medium. As a consequence, only parts of the voltage and current that satisfy the medium condition can propagate further. A fraction of the less attenuated voltage/current wave is left behind, giving rise to stored reactive power along the TL.

With a complex $\mathbf{Z}_O$, there exists standing waves even under the identical matching condition between the TL and the load, and the maximum power transfer condition is not satisfied. Under the complex conjugate matching, the reflection at the load creates an interaction between the incident and reflected waves that not only cancels out the

reactive power flow, but also restores the maximum power available from the incident wave to the load.

The understanding can be useful when designing transceivers in 5G and wireless body communication where electrical losses can cause considerable attenuation, yielding inevitable complex characteristic impedance in the communication channel. As a general guideline, if there is foreseeable adverse effect from the load reflection, such as possibility of multiple reflections by the surrounding environment or at the source, the IM condition must be employed to the trade maximum power transfer for self-interference that can disrupt the communication. If the adverse effect is negligible, the CM condition should be the design choice.

REFERENCES

[1] David M. Pozar, Microwave Engineering, 3rd ed., Wiley: New Jersy, 2005.

[2] T. S. Rappaport, et. al., "Broadband Millimeter-Wave Propagation Measurements and Models Using Adaptive-Beam Antennas for Outdoor Urban Cellular Communication," IEEE Transactions on Antenna and Propagation, vol. 21, April 2013.

[3] N. Cho et. al., "The Human Body Characteristics as a Signal Transmission Medium for Intrabody Communication," IEEE Transactions on Microwave Theory and Techniques, vol. 55, May 2007.

IEET Editorial Office

EEAAT - Electrical Engineering Academic Association (Thailand)
Room 409, F-Building
140 Cheum-Sampan Rd.
Nong Chok, Bangkok, Thailand 10530
Tel: +662-988-3655 ext 2216 Fax: +662-988-4026

www.journal.eeaat.or.th